Research Square

Preprints are preliminary reports that have not undergone peer review.
They should not be considered conclusive, used to inform clinical practice,
or referenced by the media as validated information.

# Quantitative adaptor heterogeneity sets single-cell thresholds for innate immune activation and attenuation

**Arpan Dey**
ad2327@cam.ac.uk
University of Cambridge https://orcid.org/0009-0001-0285-6879
**Yuhao Cui**
University of Cambridge https://orcid.org/0009-0007-5761-8222
**Bharti Nawalpuri**
University of Cambridge
**Georg Meisl**
University of Cambridge https://orcid.org/0000-0002-6562-7715
**Gavin Sewell**
University of Cambridge, Department of Medicine
**Abhishek Patil**
Monash University https://orcid.org/0000-0002-1087-3839
**Nurun Fancy**
Dementia Research Institute, Imperial College London https://orcid.org/0000-0002-6481-6266
**Clare Bryant**
Department of Medicine, University of Cambridge https://orcid.org/0000-0002-2924-0038
**David Klenerman**
University of Cambridge https://orcid.org/0000-0001-7116-6954

**Article**

**Keywords:**

**Posted Date:** August 27th, 2026

**DOI:** https://doi.org/10.21203/rs.3.rs-10682444/v1

**License:** This work is licensed under a Creative Commons Attribution 4.0 International License.
Read Full License

**Additional Declarations:** There is **NO** Competing Interest.

# Quantitative adaptor heterogeneity sets single-cell thresholds for innate immune activation and attenuation

Arpan Dey[1,2]§*, Yuhao Cui[1,2]§, Bharti Nawalpuri[3], Georg Meisl[1,2], Gavin W. Sewell[4], Abhishek Patil[5], Nurun N Fancy[6,7], Clare Bryant[3,8]*, David Klenerman[1,2,9]*

[1]Yusuf Hamied Department of Chemistry, University of Cambridge, Cambridge, UK
[2]UK Dementia Research Institute, University of Cambridge, UK
[3]Department of Medicine, University of Cambridge, UK
[4]Cambridge Institute of therapeutic Immunology and Infectious Disease, Department of Medicine, University of Cambridge, Cambridge, UK
[5]Monash Biomedicine Discovery Institute, Faculty of Medicine, Nursing, and Health Sciences, Monash University, Melbourne, Australia
[6]UK Dementia Research Institute Centre, Imperial College London, London, UK
[7] Department of Brain Sciences, Imperial College London, Hammersmith Hospital, London, UK
[8] Department of Veterinary Medicine, University of Cambridge, UK
[9]Lead contact
§ These authors contributed equally to this work
*Correspondence: ad2327@cam.ac.uk (A.D), ceb27@cam.ac.uk (C.B), dk10012@cam.ac.uk (D.K)

## Abstract

Macrophages exhibit a range of time-dependent responses to external stimuli, but at the single cell-level how receptor input is converted into heterogeneous inflammatory outputs, and how termination occurs remains unclear. Toll-like receptor (TLR) signaling is initiated through supramolecular protein assemblies. In this work, using macrophages with endogenously tagged myeloid differentiation primary response 88 (MyD88), and in primary mouse macrophages, we identify pre-existing heterogeneity in MyD88 abundance as a hidden single-cell variable that shapes the threshold for productive MyD88 assembly and downstream signaling. Strong agonism converts this basal heterogeneity into rapid growth of large MyD88 assemblies, robust NFκB activation, cytokine production, and induction of negative regulators. In contrast, weak agonism produces delayed and less efficient assembly, low-amplitude cytokine output, and weaker feedback engagement, resulting in persistent low-output signaling. Parallel transcriptomic analysis of Alzheimer's disease (AD) brain tissue, and blood samples across additional acute and chronic inflammatory disease cohorts, reveals a consistent, disproportionate activation-relative-to-feedback signature, suggesting incomplete activation-feedback coupling as a correlative but recurring feature of chronic inflammatory disease.

## Main

Inflammation is an adaptive response through which innate immune cells detect infection, tissue damage, or cellular stress and initiate protective programs that restore homeostasis. However, the physiological value of inflammation depends not only on how rapidly it is induced, but also on how precisely it is limited once the initiating threat has been controlled. In self-limiting inflammatory responses, pro-inflammatory signalling is progressively counterbalanced by resolution programs that are initiated early and act to restrain further signal amplification, promote clearance of inflammatory mediators, and restore tissue homeostasis[1,2]. When these regulatory checkpoints fail or remain incomplete, inflammatory activity can persist, giving rise to low-grade, chronic inflammatory states[3]. Thus, a shift from a self-limiting acute response to persistent inflammation may arise from inefficient coupling between pathway activation and its negative regulation. Whether such persistent signaling reflects pre-existing cell-to-cell differences in the mechanisms that govern activation, propagation, and termination remains poorly understood.

TLR signalling has emerged as a paradigm for understanding how innate immune recognition is converted into inflammatory output. TLR activation is commonly understood to proceed through ligand-induced recruitment of adaptor proteins such as MyD88 and TIR-domain-containing adaptor-inducing interferon-β (TRIF), which activate NFκB, mitogen-activated protein kinase (MAPK), and interferon-regulatory pathways[4–6]. More recent work has revised this linear view by showing that innate immune signalling is organized through supramolecular organizing centres (SMOCs) in which adaptor proteins assemble into higher-order complexes that amplify signalling[7,8] and impose activation thresholds[9]. MyDDosome is one such SMOC. Structural studies revealed a hierarchical death-domain assembly containing a hexameric MyD88 core. Further live-cell imaging showed that activated TLR4 transiently nucleates MyDDosome formation and that signalling strength depends on the number, size, and kinetics of these assemblies[10]. Thus, MyD88 signalling is governed by nucleation, cooperativity, and threshold-dependent assembly rather than simple adaptor recruitment. In parallel, single-cell studies have shown that inflammatory outputs are highly heterogeneous, with NFκB dynamics, and cytokine expression varying substantially between cells[11,12]. Although MyD88 assembly has been characterized extensively, and more recently under endogenous expression conditions[7], the connection between early adaptor assembly and downstream single-cell inflammatory heterogeneity remains unresolved.

In this work, we quantify endogenous MyD88 abundance across individual macrophages and show that it varies widely. Together with agonist strength, this pre-existing heterogeneity shapes the threshold for the number and kinetics of MyD88 assemblies formed in each cell. Strong stimulation and/or high MyD88 abundance promotes faster formation of larger assemblies, stronger NFκB activation, higher cytokine output, and more effective induction of negative regulation. By contrast, weak stimulation arising from either weak ligand, or low MyD88 abundance produces fewer assemblies with slower kinetics, weaker downstream signaling, and reduced feedback engagement. Using a coarse-grained analysis of MyD88 assembly, we show that strong agonism selectively biases high-MyD88 cells toward growth of

signaling-competent assemblies, a feature lost under weaker stimulation, consistent with cell-intrinsic signaling thresholds. Further at the single-cell level, inefficient coupling between activation and feedback favours persistent rather than resolved inflammatory signaling. Extending this framework to human disease, we find that inflammatory activation in AD brain tissue is similarly uncoupled from proportional negative-feedback engagement. This correlative imbalance recurs in blood transcriptomes across additional chronic, but not acute, inflammatory conditions, pointing to incomplete activation-feedback as a broader feature of chronic inflammatory disease.

**Ligand identity and dose tune heterogeneous MyD88 assembly in macrophages**

We used immortalized bone marrow-derived macrophages (iBMDMs) expressing endogenously tagged C-terminal MyD88–mNeonGreen (mNG) to monitor MyD88 assembly in living cells (**Figure 1A**). Endogenous tagging enabled detection of individual MyD88 assemblies without overexpression-related artifacts[8]. MyD88-mNG iBMDMs showed cytokine release comparable to WT BMDMs after LPS stimulation (**SI 1A**), supporting extrapolation of quantitative measurements to WT conditions. We used total internal reflection fluorescence (TIRF) microscopy for biophysical characterization of membrane-proximal, early MyD88 assemblies (**Figure 1B**). The mNG tag enabled live-cell monitoring, with assembly intensity serving as a proxy for complex size. To determine how agonist identity, dose, and time affect MyD88 assembly, we stimulated cells with three ligands across a range of concentrations (**Figure 1C**). LPS and MPLA were used to stimulate TLR4, with LPS acting as a stronger agonist than MPLA[13], whereas Pam3CSK4 was used as a potent TLR1/2 agonist[14]. The highest doses of LPS and MPLA were selected to achieve comparable cytokine output (**SI 1B**). LPS (100 ng/ml) induced a rapid ascending phase of MyD88 assembly, reaching a maximum of 28 ± 4 assemblies/cell within 20 min followed by gradual decline. In contrast, MPLA (1000 ng/ml) showed a slower, progressive rise, reaching a lower maximum of 16 ± 2 assemblies at 1 h, without a clear descending phase during the measurement period of 1 h. Pam3CSK4 (600 ng/ml) also showed delayed kinetics relative to LPS, with a maximum of 19 ± 2 assemblies at 1 h, lacking the sharp early peak-and-decay profile. Together, these differences in ascent, peak time, and decay indicate that the ligands drive distinct MyD88 assembly kinetics. Despite being a strong TLR1/2 agonist, Pam3CSK4 showed kinetics closer to MPLA than LPS, which may reflect differences in receptor organization or dimer stability between TLR4 and TLR1/2.

Quantification of ~5,000 MyD88 puncta/ligand revealed a broad range of assemblies, from monomers to hexamers and higher-order oligomers. Assembly size was approximated by comparison with monomeric MyD88-mNG intensity obtained by lysing the cells (see Methods; monomer intensity and identification in **SI 1C,D**). **Figure 1D** shows the distribution of log-transformed MyD88 assembly intensities over time after stimulation. Time-dependent broadening indicated emergence of higher-order complexes. All distributions were fitted with a sum of two Gaussians. Upon stimulation, two peaks were observed at monomer intensity and ~1.5-fold above monomer. Although distinct peaks for hexamer or higher-order

assemblies were not resolved, these larger assemblies were present throughout the time course. Detailed analysis of fits, peak positions, and population distributions is provided in **SI 1E**. We next measured the lifetime of individual MyD88 assemblies, defined as the duration for which each assembly remained visible in the TIRF field. Assemblies at or above the hexameric threshold, corresponding to the MyD88 core of the canonical MyDDosome complex[9,15,16] were operationally classified as large MyD88 assemblies, and exhibited longer lifetimes than smaller assemblies across all three ligands (lifetime fits and values in **SI 1F**). This is consistent with earlier reports of longer-lived large MyD88 assemblies[9]. The longest-lived large assemblies in our dataset were observed under Pam3CSK4 stimulation, which may reflect differences in coupling or stability between TLR1/2 and TLR4-associated assemblies. Despite their longer lifetimes, large MyD88 assemblies remained rare overall and were observed more frequently under LPS and Pam3CSK4 stimulation (up to 3 assemblies/cell) than MPLA (1 assembly/cell, **SI 1G**).

Single-cell analysis revealed marked heterogeneity in MyD88 assembly. Within the same field of view, cells with extensive assembly coexisted with cells showing very few assemblies (**Figure 1E**). Although such variability may reflect intrinsic macrophage heterogeneity, it has not previously been examined at the level of upstream events such as MyD88 assembly. Because assembly size and stability are linked to downstream signaling, we used the presence of a hexameric MyD88 assembly to stratify cells into two broad groups. The groups are not interpreted as discrete signaling states, but as an empirical framework for organizing assembly heterogeneity into analyzable pools. Cells containing at least one hexameric MyD88 assembly were assigned to Group A, and those lacking such assemblies to Group B. Group A cells also contained more total MyD88 assemblies overall, supporting this stratification (**SI 1H**). Quantification at 1 h after stimulation showed a dose-dependent increase in Group A population (**Figure 1F**). Under LPS stimulation, this increase was gradual, rising from 48.5% to 60.8% and 66.6% at 30, 60, and 100 ng/ml, respectively. In contrast, MPLA showed a delayed steeper response. Group A population remained low at 300 and 600 ng/ml (16.6% and 22.7%) and increased only at 1000 ng/ml (61.5%). A similar pattern was seen for TNFα production, with MPLA showing a steeper dose response than LPS (**SI 1B**). Together, these data suggest that downstream signaling requires crossing a threshold of productive TLR4 activation compatible with MyD88 assembly. Because MPLA lacks a backbone phosphate group, it may stabilize the TLR4 dimer less effectively than LPS[17,18], consistent with reports on other synthetic analogs[19], potentially explaining our observation.

After nucleation at TLRs, MyD88 assemblies may dissociate from the initiating receptor and persist as cytosolic signaling scaffolds[7]. We therefore asked whether assemblies across the cellular volume followed the same group stratification observed near the membrane. From this point onward, only the highest dose of each ligand was used to better contrast ligand-specific differences. Using spinning-disk confocal microscopy, we quantified total MyD88 assemblies throughout the cell volume (**Figure 1G**), with representative images of LPS, MPLA, and Pam3CSK4-stimulated cells shown in **Figure 1H**. Unlike membrane-proximal

measurements, volume analysis resolved distinct higher-order assembly peaks, likely because these could be detected separately from the membrane-associated pool, where growing monomers and small oligomers may mask them. Time-dependent intensity distributions are shown in **Figure 1I**. Quantification of individual MyD88 puncta intensities revealed predominantly hexamer-like assemblies (5.41 ± 0.38 times monomer intensity) with a few bigger complexes referred to as higher-order assemblies from here on. Fitting of the intensity distributions and resulting populations are provided in **SI 1I**.

Using the same empirical framework, we stratified cells into Groups A and B based on MyD88 assemblies across the cellular volume. **Figure 1J** shows the total number of assemblies/cell over time. Across all ligands and time points, Group A cells consistently contained significantly more assemblies than in Group B. LPS-stimulated Group A cells reached the highest assembly number earliest, peaking at 15 min (17.7 ± 1.2 assemblies/cell), whereas MPLA and Pam3CSK4 reached lower maxima (8.5 ± 1.3 and 13.1 ± 0.5 assemblies/cell) at a later timepoint of 1 h. Consistent with weaker MyD88-dependent signaling by MPLA, these results show that agonist identity is reflected in MyD88 assembly kinetics, extending earlier observations from non-endogenously tagged MyD88 systems)[10]. All three ligands showed a time-dependent decline in assembly number, consistent with TLR endocytosis and reduced MyD88-dependent signaling at longer times[10,20]. Although the population of Group A cells remained comparable across all three ligands at their highest doses across most time points (61.5 ± 11.5%; **S1J**), LPS produced the highest number of large MyD88 assemblies across most time points (**SI 1K**).

**MyD88 abundance varies widely across cells and correlates with MyD88 assembly formation**

Full-length MyD88 aggregates in a concentration-dependent manner *in-vitro* and displays a broad metastable zone for seed-catalyzed polymerization[21]. Such a metastable zone is thought to enable rapid seed-induced MyD88 signaling while preventing premature immune activation[22]. Whether a similar metastable zone exists in cells, and whether it influences MyD88 assembly, remains unknown. We therefore quantified absolute MyD88 concentration in single cells by fluorescence correlation spectroscopy (FCS)[23,24]. A schematic is shown in **Figure 2A**, confocal FCS calibration in **SI 2A**, and representative cells and FCS traces in **Figure 2B**. Traces were fitted using a 3D diffusion model to calculate MyD88 concentration in each cell (see Methods). This revealed a broad MyD88 distribution, ranging from 7 to 92 nM (**Figure 2C**). To test whether this heterogeneity is general across macrophages, we measured MyD88 expression by immunofluorescence in MyD88-mNG iBMDMs, WT iBMDMs, and primary mouse BMDMs (**Figure 2D**). Antibody specificity was validated in MyD88 knockout (MKO) iBMDMs, which showed negligible fluorescence (**SI 2B**). Quantification of the coefficient of variation (%CV = [standard deviation/mean] × 100) showed comparable heterogeneity across all three systems (32.1%, 31.2%, and 32.0% for MyD88-mNG, WT, and primary BMDMs respectively; **Figure 2E**; full distributions in **SI 2C**). The CV estimated by immunofluorescence was lower than that measured by FCS (57.4%), likely reflecting methodological differences

between fixed-cell whole-cell intensity measurements and local live-cell concentration measurements.

To examine how MyD88 heterogeneity evolves during cell division without confounding effects of migration, we seeded MyD88-mNG cells at low density on micropatterned imaging chambers containing wells separated by bioinert, non-adhesive regions (**Figure 2F**). This confined cells within defined wells (**SI 2D**), and a weak fluorescence of the bioinert surface enabled longitudinal tracking of the same local population during colony formation (details in Methods). MyD88-mNG intensity was monitored as cells divided within each well (**Figure 2G**). Heterogeneity in MyD88 abundance re-emerged in daughter cells and colonies irrespective of mother-cell intensity. Accordingly, longitudinal %CV measurements across wells showed a progressive increase in heterogeneity, reaching values comparable to FCS-based measurements at confluency (**Figure 2H**). Because cells within a colony are not synchronized in cell-cycle phase, this apparent heterogeneity could in principle arise from differences in cell-cycle state. To test this, we used Vybrant DyeCycle, a quantitative DNA-content marker (representative images in **SI 2E**). In **Figure 2I**, the two DNA-content peaks (992.3 ± 42.4 and 1874.4 ± 41.3, the latter approximately two-fold higher) correspond to G0/G1 and G2/M phases. Total MyD88 intensity from cells in each peak showed no significant difference in distribution (**Figure 2J**; see Methods for peak assignment). Thus, MyD88 heterogeneity is maintained through cell division as a cell-intrinsic feature rather than being primarily explained by cell-cycle phase.

Consistent with the concentration-dependent aggregation behaviour of MyD88 observed *in-vitro*, we next asked whether cell-to-cell variation in MyD88 abundance drives differential MyD88 assembly in individual cells. We quantified the relationship between the total normalized MyD88 intensity and number of MyD88 assemblies of the same cells after ligand stimulation. **Figure 2K** shows correlations at time points with highest MyD88 assembly/cell, with additional time-point correlations in **SI 2F**. Both Spearman and Pearson analyses revealed strong correlations under all three conditions, indicating a strong dependence of MyD88 assembly on cellular MyD88 abundance (**Figure 2K**).

**Strong agonism converts MyD88 heterogeneity into productive assembly**

MyD88 assembly is a multistep process involving TLR dimerization, ligand binding, dimer stabilisation and progressive formation of higher-order MyD88 complexes, including the hexameric core of the functional MyD88 assembly[8,10,17,25] (**Figure 3A**). Resolving individual rate constants for each step would require time-resolved measurements of all intermediates, which remain beyond current experimental reach. However, analyzing the MyD88 concentration dependence of different assembly classes under different ligand conditions can narrow the set of plausible mechanisms and provide comparative insight into assembly.

For each cell, we measured both total MyD88 abundance and the intensity of all MyD88 puncta, yielding an assembly-size distribution as a function of cellular MyD88 concentration.

For visualization, cells were partitioned into three MyD88 concentration ranges (**Figure 3B,H**), with corresponding assembly-size distributions shown in **Figure 3C–E** and **3I–K**. As MyD88 concentration increased, distributions shifted toward larger assemblies, with distinct small- and large-assembly peaks most apparent in the highest-MyD88 bins (**Figure 3E,K**). These distributions were used to define empirical cutoffs separating small and large MyD88 assemblies. For each class, we then estimated the scaling exponent with respect to MyD88 concentration from the slope of double-logarithmic plots of total assemblies/cell versus MyD88 concentration as:

$$M_S = m^{\gamma_S} \quad \& \quad M_L = m^{\gamma_L}$$

where $m$ is the monomeric MyD88 concentration, $M_S$ and $M_L$ are the concentrations of small and large MyD88 assemblies respectively, and $\gamma_S$ and $\gamma_L$ are their scaling exponents. At 15 min after LPS stimulation, small assemblies showed sublinear dependence on MyD88 ($\gamma_S \approx 0.16$), whereas large assemblies showed superlinear dependence ($\gamma_L \approx 2.68$). By contrast, under MPLA stimulation, both classes remained sublinear ($\gamma_S \approx 0.40$, $\gamma_L \approx 0.50$), a pattern that persisted at all later time points (**SI 3A–C**).

As expected, large assemblies had higher scaling exponents than small assemblies under both LPS and MPLA stimulation. However, the exponents were strikingly low, with a highest value of ~2.68. In a simple equilibrium model where hexamer formation is limited solely by free MyD88 monomers, an exponent of 6 would be expected. Even accounting for the limited resolution of our measurements, which likely group hexamers with similar-sized species, the observed values remain far below this prediction. This indicates that MyD88 abundance alone does not limit assembly formation, and that large assemblies are constrained by additional factors. FCS measurements estimated that MyD88-mNG cells contain ~12,600–831,000 MyD88 molecules (see Methods), but the number of surface TLR4 receptors are ~100–1,000[26], of which only a minority are dimeric (~22%)[10]. Additionally, differences in TLR4 dimer stabilization, together with interleukin-1 receptor-associated kinase (IRAK) recruitment, preferably to larger and more stable MyD88 assemblies[9], could further explain ligand-specific differences. A scaling exponent above 1 enhances differences in assembly number between cells with low and high MyD88 concentrations. For example, $\gamma_L \approx 2.68$ for large assemblies after LPS stimulation means that cells differing two orders of magnitude in MyD88 concentration would differ by more than five orders of magnitude in large-assembly abundance. By contrast, under MPLA stimulation, the same MyD88 difference would produce only about one order of magnitude in large-assembly abundance. Thus, strong agonism amplifies pre-existing MyD88 heterogeneity into larger differences in productive assembly, whereas weak agonism compresses those differences.

**MyD88 assembly state predicts ligand-induced NFκB activation**

Downstream of MyD88 assembly, the input signal propagates through multiple steps involving IRAKs, TRAF6, the TAK1–TAB module, and IKK complex[27]. Activation of the canonical IKK

complex enables IKKβ-mediated phosphorylation and degradation of IκBα, allowing NFκB to translocate to the nucleus (**Figure 4A**). However, nuclear translocation alone is often insufficient for gene induction. Efficient transcription also depends on inducible post-translational modification of NFκB subunits, particularly phosphorylation[28]. Multiple phospho-acceptor sites have been mapped in p65, the strongest transcriptional activator in the NFκB family, and these modifications regulate NFκB activity in a stimulus, and site-specific manner[28–30]. Nuclear accumulation of Ser536-phosphorylated p65 (Ser536-p65) therefore serves as a useful readout of downstream MyD88–IKK–NFκB signaling.

MyD88 is essential for NFκB dynamics, including nuclear translocation and oscillations[31], and MyD88-deficient macrophages show markedly reduced NFκB activity after TLR stimulation[32]. We therefore examined how MyD88 assembly relates to Ser536-p65 activity over time. Cells were stimulated with LPS or MPLA, fixed at the indicated time points, and Ser536-p65 was quantified by immunofluorescence. Representative images after LPS stimulation are shown in **Figure 4B**, and quantification for both ligands in **Figure 4C**. LPS induced a rise in total Ser536-p65 at 15 min (1.5-fold over baseline), concomitant with the rise in MyD88 assembly observed earlier, before returning to baseline by 2 h and remaining unchanged through 4 h. MPLA induced a lower rise at 15 min (**SI 4A**), after which the signal fluctuated but remained elevated above baseline up to 4 h, unlike the more transient LPS response. Thus, MPLA produced a more sustained Ser536-p65 response over the measured time window.

To visualize Ser536-p65 nuclear translocation, we generated 3D cellular models using Imaris (see Methods). A representative LPS-treated cell at 15 min is shown in **Figure 4D**. DAPI-derived nuclear masks were color-coded by total nuclear Ser536-p65 intensity, and individual MyD88 assemblies by mNG intensity. Cells with more MyD88 assemblies showed higher nuclear Ser536-p65, indicating that nuclear translocation scales with MyD88 assembly kinetics. A similar relationship was observed across all LPS time points (**SI 4B**). We then quantified Ser536-p65 nuclear translocation in Group A and Group B cells using the established stratification framework (**Figure 4E**). Fixed-cell measurements after LPS and MPLA stimulation showed detectable hexameric assemblies after fixation, allowing extension of live-cell stratification into fixed cells (**SI 4C**). Under LPS stimulation, Group A showed significantly greater nuclear Ser536-p65 enrichment than Group B, whereas Group B showed little detectable nuclear signal. The larger variance in Group A likely reflects asynchronous phosphorylated NFκB dynamics and/or multiple signaling states within this class[31,33]. By contrast, MPLA induced only weak nuclear Ser536-p65 enrichment, with no difference between groups.

To assess transcriptional output of Ser536-p65 translocation, we performed single-molecule fluorescence in situ hybridization (smFISH) for NFKBIA mRNA across the same LPS and MPLA time course (**Figure 4F**). Because the smFISH workflow disrupted mNG fluorescence, cells could not be stratified into groups, and the MyD88 channel was used only to define cell outlines (**Figure 4G**). NFKBIA is a canonical NFκB target encoding IκBα, which restores

cytoplasmic sequestration of NFκB and closes a core negative-feedback loop[34]. NFKBIA transcripts increased rapidly with LPS, from 3.9 ± 1.5 to 10.3 ± 0.6/cell at 1 h, and remained elevated through 4 h (**Figure 4H**). MPLA induced a similar increase, from 4.7 ± 0.8 to 8.9 ± 1.0 transcripts, despite much weaker nuclear Ser536-p65 translocation. Accordingly, AUC analysis showed no significant difference between LPS and MPLA (**SI 4D**). This likely reflects transcriptional selectivity downstream of Ser536-p65. Some NFκB target genes, including NFKBIA, respond broadly once the pathway is engaged, whereas others require stronger upstream p65 phosphorylation-dependent activation steps[28].

**MyD88 assembly state stratifies single-cell TNFα output**

TNF transcription is strongly dependent on NFκB activity, including stimulus-induced phosphorylation of p65, and thus provides a suitable readout to relate dynamic upstream signaling to inflammatory gene output[35]. However, in TLR4 signaling, NFκB phosphorylation is not driven solely by the early MyD88–IKK axis (observed as early as 15 min after stimulation) but also by a later TRIF-dependent phase that can contribute to TNF transcription[8,36]. We therefore measured TNFα production at 4 h, a time point expected to remain predominantly MyD88-dependent while allowing reliable cytokine detection. At 4 h, TNFα protein output is expected to reflect both de novo TNF transcription and post-transcriptional regulation of TNF mRNA stability and translation through MAPK–p38/MK2-dependent pathways[7,9,31,35]. Nevertheless, MyD88 knockout (MKO) almost completely abolished TNFα production at 4 h in MKO iBMDMs, indicating strong MyD88 dependence at this time point (**SI 5A**).

To correlate MyD88 assembly with TNFα production at the single-cell level, we added TAPI-0 to block TNFα release and TAK-242 to terminate upstream MyD88 assembly at defined time points. This allowed MyD88 assemblies formed within specific signaling windows to be related to subsequent TNFα production. The workflow is shown in **Figure 5A**. TAPI-0-mediated accumulation of membrane-anchored TNFα was measured by immunofluorescence (**Figure 5B**). Addition of TAK-242 at different time points produced differential TNFα levels across individual cells (**SI 5B**). TNFα output/cell was quantified using ring-band analysis (see Methods). TNFα production increased progressively with later TAK-242 addition, reaching a maximum at 4 h (16.11 and 4.58-fold over control for LPS and MPLA, respectively; **Figure 5C**). The broad spread in each dataset reflects heterogeneous TNFα production across cells. Unlike NFKBIA, TNFα production differed substantially between LPS and MPLA stimulation (**Figure 5C**, **SI 5C**). Pam3CSK4 stimulation was unaffected by TAK-242, serving as a negative control for assay validation (**SI 5D**). To relate MyD88 assembly to TNFα output, ΔTNFα, defined as the difference in mean TNFα between successive time points $(t_n - t_{n-1})$, was plotted with the total number of MyD88 assemblies/cell in dual-axis time-course plots (**Figure 5D,E**). Under LPS stimulation, ΔTNFα increased and began to saturate by 4 h, well after the MyD88 assembly peak at 15 min (**Figure 5D**), consistent with intervening signaling, transcriptional, and translational steps required for cytokine production. By contrast, under MPLA stimulation, ΔTNFα remained comparatively low, consistent with weaker agonism (**Figure 5E**).

At 4 h after LPS stimulation, a substantial number of MyD88 assemblies remained (4.9 ± 0.5/cell), allowing simultaneous measurement of MyD88 assembly and TNFα in the same cells. We therefore used immunofluorescence to detect both readouts, using Brefeldin A (BFA): an ER-to-Golgi trafficking inhibitor that retained TNFα intracellularly. The workflow is shown in **Figure 5F**. Although BFA reduced the dynamic range of TNFα production, LPS-treated cells still showed significantly higher TNFα intensity than untreated controls (**SI 5E**). We quantified MyD88 assembly and TNFα production in MyD88-mNG cells and primary BMDMs (**Figure 5G**). Quantification of MyD88 puncta intensity enabled group stratification in both systems, as above. In each case, Group A cells, which also contained more MyD88 assemblies, produced significantly more TNFα than Group B cells, both in MyD88-mNG cells (**Figure 5H,I**) and primary BMDMs (**Figure 5J,K**). Together, these data show that, at the single-cell level, ligand-driven TNFα output is coupled with pre-existing differences in cellular MyD88 assembly capacity.

## MyD88 heterogeneity and ligand strength couple inflammatory activation to feedback engagement

Because macrophage activation is shaped by the inflammatory stimulus, negative regulation may also vary across individual cells. Because TLR stimulation induces multiple negative regulators that terminate or restrain pathway activation, ligand identity and MyD88 abundance may jointly determine feedback engagement[37]. To test this, we compared persistence of MyD88-dependent cytokine output at early and late time points. Although MPLA induced lower absolute levels than LPS, the fraction of TNFα and IL6 remaining at 24 h relative to 4 h was significantly higher with MPLA than LPS (1.95-fold and 3.94-fold, respectively; **Figure 6A**; absolute values in **SI 6A**). Thus, LPS-induced cytokine production was more strongly dampened over time, indicative of more effective negative feedback, whereas MPLA showed weaker attenuation. Together, these data suggested that stronger agonism drives not only greater activation, but also more efficient shutdown.

We next asked whether this difference was reflected at the level of MyD88 assembly. Quantification of MyD88 assemblies in MyD88-mNG cells at later time points showed that the difference between LPS and MPLA progressively decreased, with no significant difference remaining at 24 h (**Figure 6B**). This indicated overall attenuation of signaling at later times, but did not by itself explain ligand-specific negative regulation. We therefore examined MyD88s, an exon 2-skipped isoform of full-length MyD88 (MyD88L) induced in macrophages upon prolonged inflammatory stimulation[38]. Loss of exon 2 abolishes IRAK4 recruitment and downstream signaling (**Figure 6C**), making MyD88s a candidate negative regulator of prolonged MyD88-dependent signaling[39]. In the MyD88-mNG cell line, the fluorescent tag is positioned at the C terminus, encoded by exons 3–5 (**Figure 6C**), and could therefore overestimate functional MyD88 assembly abundance at longer time points. We therefore measured MyD88s mRNA by qPCR after LPS or MPLA stimulation at 4 and 24 h. The MyD88s/MyD88L ratio increased significantly only after prolonged LPS stimulation at 24 h

(**Figure 6D**), suggesting that strong, sustained inflammatory signaling preferentially engages negative regulators such as MyD88s in a ligand-dependent manner.

Because negative regulation of MyD88 signaling occurs at multiple stages[37,40], we next asked whether it is more broadly ligand-specific. We performed bulk RNA sequencing 4 h after stimulation. Heatmaps of selected negative regulators and cytokines showing significant stimulation-induced changes, expressed as log2 fold change relative to control are shown in **Figure 6E** (raw CPM values in **SI 6B)**. LPS-treated cells showed significantly higher expression of cytokines, chemokines, and immunoregulatory genes than MPLA-treated cells. This pattern was further illustrated by the volcano plot in **Figure 6F**, and by gene set enrichment analysis, showing strong positive enrichment of inflammatory pathways under LPS stimulation (**SI 6C**). Together, these results indicate that LPS engages a broader inflammatory and regulatory transcriptional program than MPLA.

Because signal induction reflected combined effects of MyD88 heterogeneity and ligand identity, we next asked whether intrinsic differences in MyD88 abundance also drive cell-to-cell variation in induction of negative regulation. Among the negative regulators identified by bulk RNA sequencing, TNFAIP3, which encodes the well-characterized inhibitor A20, differed significantly between LPS and MPLA-stimulated cells (**Figure 6F**). We therefore measured ligand-induced A20 production in single cells by immunofluorescence (**Figure 6G**). A20 levels were significantly higher after LPS than MPLA stimulation, consistent with the RNA-sequencing results (**SI 6D**). Stratification of LPS-treated cells by MyD88 puncta intensity further revealed a quantitative difference in A20 production, with Group A cells producing ~30% more A20 than Group B cells (**Figure 6H**).

**Inflammatory activation without proportional transcriptional feedback engagement is a conserved feature of AD pathology and chronic inflammatory diseases**

Our macrophage data identified that under weak agonism, inflammatory activation becomes uncoupled from proportional negative-feedback engagement, resulting in a persistent low-amplitude inflammatory signaling. Since sustained, low-grade inflammatory states are a recurring pathological feature of chronic inflammatory diseases, we asked whether inflammatory activation and its negative regulation become similarly imbalanced in chronic human disease. As a first test, we utilized data from dorsolateral prefrontal cortex (DLPFC) tissue of a large-scale *postmortem cohort* comprising AD cases along with non-disease control[41]. We examined whether microglial activation occurs across AD progression stage (Braak stage), or in AD-associated pathology (amyloid-β burden, and tau burden), and whether pathology-linked inflammatory activation is accompanied by proportional transcriptional feedback and negative-regulatory engagement. Using bulk and single-nucleus RNA sequencing (snRNAseq) (**Figure 7A**), we tested the association between AD neuropathology and the expression of activation and feedback-associated transcripts identified from our macrophage system.

MYD88s reports the receptor-proximal TLR/MyD88 axis[39,42], NFKBIA marks NFκB pathway engagement[34], and TNFAIP3/A20 and SOCS3 represent negative-regulatory axes linked to NFκB[43] and cytokine/JAK–STAT[44] signaling respectively. Additional MAPK and RNA-regulatory feedback genes, including DUSPs[45] and ZC3H12A[46], are shown in **SI 7A**. In bulk cortical tissue, NFKBIA showed the strongest association with increasing Braak stage (ANOVA *p-value* = 0.000111), consistent with progressive NFκB-linked inflammatory activation in AD brain tissue[47] (**Figure 7B**). To test this association more robustly, we performed a regression analysis of gene expression against Braak stage as the predictor variable while adjusting for known covariates including sex, age at death, and APOE genotype status. NFKBIA showed a significantly positive association with Braak stage (adjusted *p-value* = 0.008). In contrast, MYD88s, TNFAIP3/A20, and SOCS3 did not scale proportionally with Braak stage, suggesting that pathology-associated inflammatory activation is not matched by coordinated transcriptional engagement of broader negative-regulatory programs. Cytokine and chemokine transcripts as identified from the macrophage results did not show any associations with Braak stage (**SI 7B**), likely reflecting their transient and post-transcriptionally regulated nature and the limited ability of bulk-tissue mRNA to capture secreted inflammatory outputs. Further we examined whether this pathology-linked inflammatory signature identified in bulk cortical tissue was reflected in microglia. At least half of the transcripts of our gene of interest are expressed in a minimum of 5% microglia nuclei from snRNAseq data indicating engagement of these pathways in microglia (**SI 7C**). Consistent with bulk RNAseq, NFKBIA showed positive associations with Braak stage (*p-value* = 0.00034) (**Figure 7C**), amyloid-β burden (**Figure 7D**), and tau tangle burden (**Figure 7E**). In contrast, broader negative regulators, including TNFAIP3/A20, MYD88s, and SOCS3, did not show comparable associations with Braak stage, amyloid-β, or tau pathology (**Figures 7C–E**; DUSPs and ZC3H12A in **SI 7D–F**). Notably, NFKBIA transcripts did not correlate with total microglial abundance (**SI 7G**), suggesting that its association reflects pathology-linked inflammatory activation rather than microglial density alone.

Having identified this uncoupling in AD brain tissue, we next asked whether it reflects a general feature of chronic inflammatory disease. We therefore examined publicly available peripheral blood transcriptomic datasets spanning chronic and acute inflammatory diseases and infections (cohort detail in methods). Chronic conditions included mild cognitive impairment (MCI), Parkinson's disease (PD), amyotrophic lateral sclerosis (ALS), Crohn's disease (CD), and ulcerative colitis (UC) (**Figure 7F**), while acute conditions included influenza, spinal cord injury (SCI), COVID-19, sepsis, and septic shock (**Figure 7G**). We calculated scaled Z-score values for a selected set of genes across all cohorts (see methods). Across chronic conditions, inflammatory activation markers including NFKBIA, TLR2, IL1B, and PTGS2 were broadly elevated, while negative-feedback regulators such as TNFAIP3, SOCS3, and ZC3H12A remained comparatively low (**Figure 7F-G, $log_2$FC values in SI 8A-B**). Acute inflammatory and infectious conditions showed more proportional/higher feedback transcripts over activation (**Figure 7G**). To quantify this directly, we calculated a composite index for each condition

(mean Z-score of inflammatory genes minus mean Z-score of negative genes; **SI 8C,D**) and compared it between chronic and acute datasets. Chronic conditions showed a significantly higher uncoupling index in terms of negative feedback genes than acute conditions (**Figure 7H)**.

## Discussion

Cell-to-cell heterogeneity has long been implicated in shaping differential immune responses, and single-cell studies have shown that NFκB activation can vary markedly across apparently similar cells in its timing, amplitude, and persistence[11,12]. Our results place an important part of this variability further upstream, showing that TLR agonists act on a non-uniform macrophage population with a pre-existing distribution of cellular MyD88 states. This distribution is likely maintained within a productive range, as excessive MyD88 can promote aberrant signaling[48,49], whereas insufficient MyD88 can weaken downstream inflammatory signaling and favour immune suppression[50]. Our results show that macrophages span an approximately order-of-magnitude range in MyD88 abundance, and together with agonist strength this determines whether individual cells enter a signaling-competent assembly state. Operationally, this can be captured by stratifying cells by the presence of large MyD88 assemblies, with high-MyD88 cells entering this state more readily than low-MyD88 cells (only in the presence of strong agonism or high dosage of weak ligands). This heterogeneity was stable rather than transient, re-emerging after cell division independently of cell-cycle state. Subsequently, the relative abundance of fast and slow-response states converted distinct inputs into graded analog outputs.

Such stable heterogeneity also helps explain the assembly mechanism itself. Recent work on death-fold signaling proteins has shown that many innate immune adaptors carry sequence-encoded nucleation barriers, allowing them to remain soluble above their saturation concentration and to assemble abruptly once seeded[51,52]. However, the presence of small MyD88 assemblies in unstimulated cells argues that MyD88 assembly is not fully explained by a purely nucleation-barrier-limited supersaturated state. Instead, our data suggest that the probability of forming signaling-competent MyD88 assemblies in a cell is shaped by several factors, including absolute MyD88 abundance, nucleation-competent TLR dimers, and downstream steps such as IRAK recruitment into growing assemblies. In this framework, pre-existing MyD88 heterogeneity biases the relative distribution of assembly states. Enrichment of large assemblies in high-MyD88 cells under strong agonism indicates that productive assembly is selectively promoted in a MyD88-dependent manner, even if other pathway components covary with MyD88 abundance. This also explains why excessively high MyD88 could, in principle permit stimulus-independent signaling from a small basal pool of receptor dimers[48,49].

Importantly, group stratification based on MyD88 assembly also predicted both downstream signal transduction and negative regulation. Under LPS stimulation, the fast-response, high-assembly state cells showed greater nuclear enrichment of Ser536-p65 and higher TNFα

production than the slow-response state. By contrast, MPLA produced weak Ser536-p65 nuclear translocation and uniformly low TNFα in both groups. However, a broadly comparable *NFKBIA* induction under LPS and MPLA suggested that some NFκB target genes respond once the pathway is engaged, whereas others, such as *TNFα*, are more sensitive to the strength and quality of upstream MyD88-dependent signaling. The stronger inflammatory signaling induced by LPS produced not only broader transcriptional activation of cytokines and chemokines, but also stronger attenuation at later time points, accompanied by increased induction of negative regulators such as MyD88s and immunoregulatory programs involving TNFAIP3/A20, SOCS3, NFKBIZ and ZC3H12A. By contrast, MPLA showed little or significantly weaker induction of these negative modulators and was associated with persistent low-amplitude cytokine production even at 24 h, consistent with a weakly resolved inflammatory state exhibiting features reminiscent of chronic inflammation.

Our earlier finding that amyloid-β (Aβ) aggregates induce slower MyD88 assembly kinetics in macrophages, albeit in an overexpression system[53], is consistent with broader evidence that misfolded protein aggregates can act as weak agonists for microglia, driving pro-inflammatory cytokine production[54]. In addition, growing evidence implicating innate immune genes in chronic neuroinflammation prompted us to ask whether persistent inflammatory activity in AD may reflect not only sustained pathway activation, but also insufficient proportional engagement of negative-regulatory programs[55,56]. Using bulk and snRNAseq data from a large-scale published post-mortem cohort[41], we found a Braak stage-dependent increase in inflammatory signaling in DLPFC tissue without coordinated transcriptional induction of negative-regulatory program. In microglia-specific transcriptomes, several negative regulators were detectable, but unlike NFKBIA, they did not track with Braak stage or amyloid and tau burden. This is notable because A20/TNFAIP3 and SOCS3 are important brakes on neuroinflammatory microglial activation[57–61]. Although several of these feedback regulators are further controlled by post-transcriptional and translational modifications, their dynamic regulation and rapid turnover makes sustained transcription an important requirement for maintaining an effective negative feedback[62–66]. Thus, an absence of proportional induction of these regulators with increasing pathology in AD-associated inflammatory activation is consistent with weak agonism by Aβ aggregates. This is particularly significant because NFκB and type I interferon signaling converge downstream of multiple innate pathways implicated in AD (including cGAS–STING)[67-69], raising the possibility that incomplete negative-feedback engagement reflects a shared vulnerability that can extend beyond the MyD88–TLR axis. Extending this analysis to peripheral blood transcriptomes, we found that this uncoupled pattern recurred across additional chronic conditions, including further neurodegenerative disease and inflammatory bowel disease. However, a proportional or slightly enhanced engagement of such feedback transcripts in acute inflammatory and infectious diseases might contribute to their self-limiting nature.

In summary, our results provide a mechanistic framework for how macrophages sustain heterogeneous MyD88 abundance to shape single-cell inflammatory decision-making,

enabling both graded signal initiation and distinction between self-limiting and persistent modes of inflammation. Although the concordance between human clinical datasets and our *in vitro* mechanistic findings is compelling, longitudinal *in vivo* validation in patient cohorts will be essential to validate our findings across disease progression. Additionally our work opens a broader line of questions regarding whether similar mechanisms occur in signalling by other innate immune signalosomes[8,70].

**Resource availability**

Lead Contact: Additional information and requests should be directed to David Klenerman (dk10012@cam.ac.uk).

Materials availability: The MyD88 mNG iBMDMs used in this study have already been described[8]. The MyD88 knockout iBMDM line generated in this study is available upon request to the lead contact.

Data and code availability: Bulk RNAseq data (differential-expression results) for unstimulated, LPS, and MPLA stimulated macrophages are provided as additional supplementary files. The raw data files are deposited in NCBI GEO available under accession number GSE336686. Source code and documentation for tracking individual MyD88 assembly, intensity, and lifetime analysis are available at https://github.com/zeroth/simple_particle_tracking. ROSMAP metadata from https://www.synapse.org/Synapse:syn3219045 was used for Bulk and snRNAseq analysis. All other data, and additional information will be shared by the lead contact upon request.

**Acknowledgements**

We gratefully acknowledge Dr Marcus Taylor (Max Planck Institute for Infection Biology, Germany) for providing bones from a male MyD88–mNeonGreen transgenic mouse, and Prof. Kate Fitzgerald (UMass Chan Medical School, USA) for generating the immortalized bone marrow-derived macrophages (iBMDMs). We also thank the imaging facility at the Cambridge Institute for Medical Research (CIMR) for providing access to their FCS set-up, data-analysis work station, and software. We are grateful to Prof Nick Gay (Department of Biochemistry, University of Cambridge, UK) for critically reading the manuscript and providing constructive feedback. All the cartoons, and figure alignment were done in https://BioRender.com.

**Funding**: This work was supported by ARUK grant ARUK-PG2020A-009 (C.B. and D.K.), Astex-DRI grant (D.K. and C.B.), UKDRI grant UKDR-2201 (D.K.), Royal Society (Research Professorship RP150066 to D.K.). D.K., and A.D. also acknowledges support from ARUK-PPG2025-023 grant. G.W.S. is funded by Wellcome Early Career Award 227584/Z/23/Z. N.N.F. is an Edmond and Lily Safra Fellow supported by the Edmond J. Safra Foundation.

**Author Contribution:** A.D., C.B., and D.K. conceived the study. A.D. and Y.C. designed the experiments with input from C.B. and D.K. A.D. and Y.C. performed and analyzed the live-cell and fixed-cell MyD88 imaging experiments. A.D. performed FCS measurements, MyD88

abundance analyses, NFκB activation assays, TNFα measurements, and immunofluorescence experiments. Y.C. performed the smFISH experiments. A.P., A.D, and Y.C. contributed to quantitative image-analysis pipelines. B.N. and G.W.S. contributed to primary BMDM culture, B.N. analysed the *in vitro* bulkseq measurements, and immunological assays with assistance from A.D. and Y.C. G.M. contributed to the conceptual development and interpretation of the coarse-grained scaling analysis. N.N.F. performed transcriptomic analysis of the human AD dataset. A.D. performed transcriptomic analysis of the other human inflammatory diseases. A.D. performed data visualization and prepared the figures with input from Y.C., B,N., G.M., N.N.F., C.B., and D.K. C.B. and D.K. supervised the work and provided project administration and funding acquisition. A.D. wrote the original draft of the manuscript. All authors contributed to reviewing and editing the manuscript and approved the final version.

**Declaration of interests:** The authors declare no competing interests.

**Declaration of generative AI in the writing process:** During the preparation of this work, A.D. used ChatGPT to improve the readability and language of the manuscript. After using this tool, the authors reviewed and edited the content as needed, and take full responsibility for the content of the published article.

## Methods

### Cell lines and culture

All cell lines (MyD88–mNG, WT, and MyD88 knockout iBMDMs) were cultured in Dulbecco's Modified Eagle Medium (DMEM) supplemented with 10% fetal bovine serum, 2 mM L-glutamine, 1 mM sodium pyruvate, 100 U/mL penicillin, and 100 µg/mL streptomycin. Cells were maintained at 37 °C in a humidified atmosphere containing 5% $CO_2$ and were expanded up to passage 8 prior to experimental use.

Bones from a male MyD88–mNG transgenic mouse were generously provided by Dr. Marcus Taylor (Max Planck Institute for Infection Biology, Germany). Bone marrow cells were isolated and subsequently immortalized via J2 retrovirus by Prof. Kate Fitzgerald (UMass Chan Medical School, USA) to generate immortalized bone marrow-derived macrophages (iBMDMs).

### Primary Bone marrow derived macrophage (BMDM) culture

C57BL/6N mice (6–12 weeks old, age- and sex-matched) were sourced from specific pathogen-free colonies at the Central Biomedical Services (CBS) facility, University of Cambridge, all animal procedures were approved by the UK Home Office and conducted in accordance with institutional ethical standards. Bone marrow cells were isolated by flushing femurs and tibias with PBS, filtered through a 70 µm strainer, and resuspended in complete RPMI-1640 (10% FBS, 100 U/mL penicillin-streptomycin, 1 mM HEPES), then plated and differentiated into BMDMs over 6 days in the presence of 100 ng/mL M-CSF, with medium refreshed on day 3. Mature BMDMs were detached by harvesting in to sterile PBS containing 10mM EDTA and 4mg/ml lidocaine-HCl, and replated at 0.3 × 10^6 cells onto well chambers (8 well high:ibidi

GmbH, catalog no. 80806), maintained in DMEM (10% FBS, 100 ng/mL M-CSF), and stimulated with the specified agonist as detailed in relevant figure legends.

**CRISPR–Cas9 genome editing**

*Myd88* knockout (Mko) iBMDMs were generated using CRISPR–Cas9 genome editing. A guide RNA (crRNA: 5′-GGTTCAAGAACAGCGATAGG-3′) targeting the first exon of *Myd88* was designed using the CRISPOR tool. Ribonucleoprotein (RNP) complexes were assembled by annealing 400 pmol crRNA with 200 pmol tracrRNA (IDT) at 95 °C for 5 min, followed by cooling to room temperature. Cas9 protein (366 pmol) and 4 µM electroporation enhancer were then added and incubated for 15 min at room temperature. The RNP mixture was nucleofected into $1*10^6$ wild-type iBMDMs using the Nucleofector 2b device (program Y-001) and the Lonza Nucleofector KitV. Transfected cells were plated in 6-well plates containing DMEM supplemented with 10% FBS and allowed to recover prior to bulk population screening.

Single-cell clones were obtained by limiting dilution (10 cells/mL in 96-well plates). Genomic DNA from individual clones was extracted, and the targeted region was amplified by PCR and analyzed by Sanger sequencing. Sequencing chromatograms were evaluated using the Synthego ICE tool to confirm clonality and knockout efficiency. Verified *Myd88*-deficient clones were expanded and characterized phenotypically. Guide RNA and locus-specific PCR primers used for sequencing are listed in Table S1. All oligonucleotides were synthesized by Integrated DNA Technologies (IDT) and used without further purification. Primer sequences flank the CRISPR–Cas9 target site within *Myd88* exon1, with the forward primer used for both PCR amplification and Sanger sequencing.

| Target | Type | Sequence (5′→3′) | Application | Source |
|---|---|---|---|---|
| *Myd88* | crRNA | GGTTCAAGAACAGCGATAGG | Guide RNA targeting exon 1 | IDT |
| *Myd88* | tracrRNA | Standard tracrRNA (Alt-R) | RNP complex assembly | IDT |
| *Myd88* | Forward primer | AAGCACGTTTCCTCACCGAT | PCR amplification and Sanger sequencing of target locus | This study |
| *Myd88* | Reverse primer | CAGATGCCAGAGGCGGTTTA | PCR amplification of target locus | This study |

**RNA isolation, cDNA prep and qPCR**

Total RNA was extracted from homogenized lysates using the PureLink™ Mini RNA Isolation Kit (Cat. No. 12183018A, Thermo Fisher Scientific). Complementary DNA (cDNA) was synthesized from the isolated RNA using the QuantiTect Reverse Transcription Kit (Cat. No. 205311, Qiagen). Quantitative PCR (qPCR) was carried out on a Bio-Rad CFX384 real-time thermal cycler using PowerTrack™ SYBR Green Master Mix (Cat. No. A46109, Thermo Fisher Scientific) and gene-specific primers.

| Transcript | Forward primer (5’-3’) | Reverse primer (5’-3’) |
|---|---|---|
| **GAPDH** | CAACTCCCTCAAGATTGTCAGCA | GGCATGGACTGTGGTCATGA |
| **Myd88-L** | CCACCCTTGATGACCCCCTAGGACAAAC | GTCTGTTCTAGTTGCCGGATCATCTCCTGCAC |
| **Myd88-S** | GGAGCTGAAGTCGCGCATCGGACAAAC | GTCTGTTCTAGTTGCCGGATCATCTCCTGCAC |

**Bulk RNA sequencing experiments**

For bulk RNA-seq, 300,000 MYD88–mNeonGreen cells were seeded per well in 48-well plates on the day of the experiment in fresh culture medium. After 4 hours, cells were stimulated with either lipopolysaccharide (LPS, 100 ng/mL) or monophosphoryl lipid A (MPLA, 1,000 ng/mL) for the 24-hour time point. The following day, a separate set of wells was stimulated for 4 hours under the same conditions, after which conditioned media from both the 4-hour and 24-hour treatments were collected, and cells were lysed directly in 50 µL/well of Zymo PureShield lysis buffer. Lysates were mixed thoroughly, transferred to 8-strip tubes, and submitted to Plasmidsaurus for single-end 3’ RNA sequencing on the Illumina platform using their internal RNA-seq analysis pipeline based on edgeR. Differential expression analysis was performed within this pipeline, and genes with $\log_2$ fold-change ≥ 1 and adjusted p-value ≤ 0.05 were considered significantly differentially expressed, with p-values adjusted for multiple testing.

**Cytokine Quantification (ELISA)**

Cytokine concentrations in cell culture supernatants were quantified by enzyme-linked immunosorbent assay (ELISA) following appropriate dilution of samples in growth media and processing according to the manufacturers’ protocols. Cells were seeded at a density of 150,000 cells/well in 48 well plates and incubated in growth media with ligands for 4hrs, and 24 hrs respectively. TNFα levels were measured using the Mouse TNFα DuoSet ELISA (DY410, R&D Systems), and IL-6 levels using the Mouse IL-6 DuoSet ELISA (DY406, R&D Systems). Assays were performed in half-area 96-well plates using 50 µL of supernatant per well for DuoSet assays, and in the pre-coated plates provided with the IFNβ kit according to the manufacturer’s instructions; absorbance was recorded at 450 nm with reference correction at 570–590 nm on a BMG LABTECH microplate reader. Cytokine concentrations were calculated from standard curves generated with recombinant cytokine standards supplied with each kit.

**TIRF Microscopy (imaging live cell MyD88 assembly)**

Live imaging of MyD88 mNG cells was carried out in a custom-built TIRF microscope. The microscope was fitted with incubator to maintain temperature at 37°C for long-term imaging. A 488-mm laser line (iBeam smart, Toptica) was used to excite mNG and visualize MyD88 assembly. In the setup, the beam was expanded using Galilean beam expanders and focused

to the back focal plane of the objective using Köhler lens to generate a Gaussian illumination profile. A 100× objective was mounted on an inverted optical microscope (Ti2 Eclipse, Nikon Corporation), and the Nikon perfect-focus system was used to maintain focus throughout image acquisition. The image acquisition was controlled through Micro-Manager 2.0, while laser powers were controlled through the use of the manufacturer's software, or by attenuation using neutral density filters. Exposure times and laser powers were set for each experiment such as to minimize any unwanted photobleaching, while maximizing the acquired fluorescence signal. The TIRF angle was controlled by precise movement of a XY translation stage with mirrors that focused the 488 excitation at the back focal plane of the objective lens. The system was calibrated using 0.1 µm Tetraspeck microsphere beads (Invitrogen) often to check alignment. The fluorescence emission was cleaned by suitable emission filters (FF01-520/44-25 + BLP01-488R, Semrock), and was recorded using an electron-multiplying charge-coupled device with an EM-gain of 250 ADU/photon (Evolve 512 Delta EMCCD, Teledyne Photometrics). The image acquisition was controlled through Micro-Manager 2.0.

**Volumetric imaging of live and fixed cells**

Confocal imaging of MyD88-mNG cells was performed using two microscope configurations. Laser-scanning confocal imaging was performed on a Zeiss LSM 780 confocal microscope equipped with an environmental incubation chamber providing temperature and $CO_2$ control. Spinning-disk confocal imaging was performed on a 3i spinning-disk confocal microscope equipped with a Yokogawa CSU-W1 SoRa confocal scanner unit and a 3i mSwitcher millisecond optical switching module. The spinning-disk system was not equipped with environmental $CO_2$ or temperature control; therefore, imaging of live cells on this system was performed over short acquisition periods in pre-warmed imaging medium.

For both microscope systems, cells were imaged using a 100× oil-immersion objective. MyD88–mNG was excited using the 488 nm laser line, and fluorescence emission was collected using an appropriate emission filter or spectral detection window. For the Zeiss LSM 780 system, emission was collected using the confocal detector (high-sensitivity GaAsP) with the pinhole set to 1 Airy unit. For the 3i spinning-disk system, fluorescence was collected through the CSU-W1 SoRa spinning-disk scanner onto the camera detector (back-illuminated SCMOS, Teledyne Prime 95B). Laser power, exposure time, binning, z-step size, and acquisition interval were kept constant across experimental conditions.

For quantitative imaging, acquisition settings were chosen to avoid pixel saturation while preserving sufficient signal-to-noise for detection of MyD88–mNeonGreen puncta. Unstimulated and stimulated samples were imaged using matched acquisition parameters within each experiment. Quantitative comparisons were made between samples acquired under identical microscope settings and, where data from both microscopes were analysed together, microscope system identity was accounted for during analysis or data were normalized within each imaging system.

## MyD88 assembly live-cell imaging

MyD88-mNG cells were plated onto glass-bottom confocal dish (ibidi GmbH, catalog no. 81156) or well chambers (8 well high:ibidi GmbH, catalog no. 80806, 18 well high: ibidi GmbH, catalog no. 81816) and left to adhere overnight. The complete DMEM was then replaced by FluoroBrite complete DMEM [FluoroBrite DMEM, 10% FBS, 2 mM l-glutamine, 1 mM sodium pyruvate, penicillin (100 U/ml), and streptomycin (100 µg/ml)] containing 25 mM Hepes. MyD88-mNG were stimulated by adding LPS, MPLA, or $Pam_3CSK_4$ at required dosage, and were imaged in TIRF or confocal. In TIRF, the focus plane was set to the bottom surface of cells, and one frame was captured in the same field of view (FOV) at required interval. For confocal measurements, 3D stacks were obtained with a z-step of 0.5 µm. The z-stacks were converted into maximum intensity projections. Image analysis was performed using Fiji (National Institutes of Health) with a custom automation macro. All images were first background-subtracted by Gaussian blurring (radius = 4 pixels). MyD88 puncta were identified using ThunderSTORM, and their intensity was subsequently measured. Puncta were distinguished from noise by having twofold intensity significance compared to the background.

## MyD88-mNeonGreen photobleaching

One-milliliter MyD88-mNG suspension (cell concentration = $10^7$ cells/ml) was centrifuged at 4°C, 400*g* for 5 min to collect cell pellets. The pellets were washed twice with 3 ml of ice-cold PBS and then resuspended in 500 µl of lysis buffer (50 mM tris-HCl, 150 mM NaCl, and 1% NP-40, pH 7.4) containing protease inhibitors (Complete Roche, catalog no. 4693116001) and phosphatase inhibitors (PhosSTOP Roche, catalog no. 4906845001). The mixture was incubated on ice for 30 min and centrifuged at 4°C, 16,000 rpm for 30 min to remove cell debris. The supernatant (200 µl) was transferred into a glass-bottom eight-well chamber (ibidi GmbH, catalog no. 80807) and imaged in TIRF. A total of 1000 frames were continuously captured at the same FOV, with an exposure time of 100 ms to achieve photobleaching. Monomeric MyD88-mNG proteins were identified by a single intensity drop in the photobleaching intensity curves, and their intensity was determined using the same method as in MyD88 puncta.

## Single Molecule RNA Fluorescence *in situ* Hybridisation (smRNA-FISH)

A total of 50,000 MyD88-mNG cells were plated in 18-well chamber slides (ibidi, 81817) and cultured overnight before stimulation with 100 ng/mL LPS or 1000 ng/mL MPLA. Cells were then washed once with PBS and fixed with 4% (w/v) paraformaldehyde (Thermo Fisher Scientific, 28906) for 20 min at room temperature. Residual paraformaldehyde was quenched with 0.1 M glycine in PBS, followed by two washes with PBS. *NFKBIA* mRNA was detected using the ViewRNA ISH Cell Assay Kit (Thermo Fisher Scientific, QVC0001) together with the ViewRNA Type 6 Probe Set for mouse *NFKBIA* (Thermo Fisher Scientific, VB6-11427) according to the manufacturer's protocol.

Fluorescence images were acquired using a spinning-disk confocal microscope equipped with a 100× objective and 2×2 pixel binning. MyD88-mNG protein was imaged using 488-nm laser excitation with 200 ms exposure, gain = 3, and 100% laser power, while *NFKBIA* mRNA was imaged using 640-nm laser excitation with 50 ms exposure, gain = 1, and 30% laser power. Z-stack images were acquired from the bottom to the top of cells with a step size of 0.3 µm. Acquired image stacks were z-projected into a single plane, using average intensity projection for the MyD88-mNG channel and maximum intensity projection for the *NFKBIA* channel. Cells were segmented in the MyD88-mNG channel using the StarDist plugin with a score threshold of 0.6 and an overlap threshold of 0.3. *NFKBIA* mRNA signals were detected using the ThunderSTORM plugin, with signals distinguished from background noise using a detection threshold of three times the standard deviation of the background intensity.

**Lifetime analysis of MyD88 assembly (Image Analysis and Particle Tracking)**

A custom Python pipeline was developed to detect and track fluorescent particles across time-lapse image stacks. The pipeline consisted of three sequential stages: (i) per-frame background removal and blob detection to produce object masks and per-object region properties, (ii) frame-to-frame linking of detected objects into trajectories, and (iii) downstream quantification of track length and intensity distributions. Source code and documentation are available at [https://github.com/zeroth/simple_particle_tracking]. Analysis was performed with Python 3.x using scikit-image, trackpy, NumPy, pandas, tifffile, and matplotlib.

*Image pre-processing and particle segmentation*

Multi-frame TIFF stacks were read with *tifffile*[71] and each 2D frame was processed independently. Uneven background and slowly varying illumination were suppressed by grayscale morphological reconstruction by dilation[72,73], which estimates a smooth background image from a seed obtained by erosion of the frame with a disk-shaped structuring element (default radius 10 pixels) and subtracts it from the original frame. This preserves compact bright features while removing diffuse background.

Candidate particles were detected on the background-subtracted frames using multi-scale Laplacian-of-Gaussian (LoG) blob detection[74]. Each frame was rescaled to the intensity range [0, 1] prior to detection. Blobs were identified as local maxima of the scale-normalised LoG response across a range of Gaussian scales σ sampled logarithmically; overlapping and border-touching detections were discarded. Values of σ and the response threshold were tuned to the expected particle size and signal-to-noise ratio of each dataset (typical values: σ = 2–10 px, threshold = 0.09).

Each detected blob, parameterised as a centre (y, x) and scale σ, was rasterised onto a binary mask as a disk of radius $\sigma \cdot \sqrt{2}$ (the characteristic radius of a Gaussian spot matching a LoG response at scale σ). The mask was then connected-component labelled and per-object region

properties — area, centroid, mean/max/min intensity (measured on the original frame), bounding box, equivalent diameter, perimeter, and solidity — were extracted. Background subtraction, blob detection, and region-property extraction were performed with scikit-image[75]. Per-frame detection and property tables were concatenated into a single table with an explicit frame index.

Segmentation of image stacks was parallelised across frames using a thread pool (one worker per available CPU core by default), and output masks were written directly to a memory-mapped TIFF to allow processing of stacks too large to hold in RAM.

*Particle linking and trajectory reconstruction*

Per-frame detections were linked into trajectories across frames using *trackpy*[76]. A maximum search radius of *search_range* pixels between consecutive frames and a gap-closing *memory* of *M* frames (i.e., a particle was permitted to disappear for up to M frames before being declared lost) were used; default values of *search_range = 2* px and *memory = 3* frames were adjusted based on the observed particle density and displacement statistics of each experiment. Linking produced per-detection particle identifiers, from which a track table (one row per detection, grouped by particle) was assembled.

*Trajectory post-processing and quantification*

Track length was defined as the number of frames in which a particle was detected after linking, computed as the per-particle count in the track table. Per-track intensity was summarised by the maximum over frames of the mean intensity within the segmented particle mask. For visualisation, per-track maximum intensities were min–max normalised to [0, 1] across the dataset. Distributions of track length and normalised per-track maximum intensity were visualised as histograms. For MyD88 puncta lifetime measurements, images were acquired under TIRF illumination with an exposure time of 100 ms and a frame interval of 30 s. Because images were collected every 30 s, lifetimes shorter than 30 s could not be resolved and were limited by the temporal resolution of the acquisition.

*Software and data availability*

The segmentation and tracking pipeline is implemented in two command-line Python modules (*segment.py* and *tracking.py*) and a companion Jupyter notebook for downstream analysis. All parameters used to produce the reported results are recorded in the analysis notebook and are reproducible from the raw TIFF stacks.

**Fluorescence correlation spectroscopy (FCS)**

Intracellular MyD88–mNG concentration was quantified in live cells using confocal fluorescence correlation spectroscopy on a Zeiss LSM 780 laser-scanning confocal microscope equipped with an FCS module and an environmental incubation chamber for temperature and $CO_2$ control. During measurements, cells were maintained at 37°C and 5% $CO_2$ in imaging medium as described previously. Similar to the live cell imaging protocol, the cells were

seeded onto glass bottom confocal dish dish (ibidi GmbH, catalog no. 81156) at a density of 0.3 × 10^6 cells and left to adhere overnight.

mNG was excited using the 488 nm laser line, and fluorescence emission was collected using a detection window of 491-633 nm. FCS measurements were acquired using a 40X water immersion objective with numerical aperture of 1.2. Laser power was kept low (3% of the power range in Zen software) to minimize photobleaching and phototoxicity while maintaining sufficient photon counts for autocorrelation analysis. Signal was detected using the high-sensitivity GaAsP detector of the Zeiss LSM 780 in photon-counting mode. The detector was configured for single-point FCS measurements, and fluorescence intensity fluctuations were autocorrelated using the Zeiss ZEN/FCS analysis module. However the raw data was extracted and separated using a fitting model with 3d diffusion of one fluorescent component with a triplet fluctuation. The equation is as follows

$$G(\tau) = 1 + \frac{1}{N}\left(1 + \frac{T}{1-T}e^{\frac{-\tau}{\tau_T}}\right)\left(1 + \frac{\tau}{\tau_{diff}\kappa^2}\right)^{-1/2}$$

- $N$ - average number of fluorescent molecules in observation volume
- $\tau diff$ - diffusion times of fluorescent species
- $\kappa$ - structure parameter (axial:lateral waist ratio) of observation volume
- $T$ - triplet fraction
- $\tau T$ - triplet relaxation time

Correlation was carried out for 30 sec with a binning of 0.2 µs. Before cellular measurements, the confocal detection volume was calibrated using a freely diffusing solution (50 nM and 100 nM) of Alexa Fluor™ 488 Succinimidyl ester (Thermofisher, catalog no. A20000) prepared in PBS. Calibration measurements were acquired using the same optical configuration as used for cellular FCS, at 37°C. The effective confocal volume (0.5-0.7 femtolitre) was determined from the fitted average number of fluorescent molecules in the detection volume and the known dye concentration. The diffusion coefficient D was calculated to be 690 $\mu m^2$/sec, within the range of reported literature with Stoke-Einstein scaling. Only calibration measurements with stable count rates and well-fitted autocorrelation curves were used for subsequent concentration calculations.

For cellular FCS, individual cells were first identified by confocal imaging the unstimulated cells. The FCS observation volume was positioned within the cytoplasm of single cells using Spot Select (crosshair) module in Zen, avoiding the nucleus, cell edges, and any visible MyD88 puncta. This strategy was used to estimate the local concentration of the diffuse cytoplasmic MyD88–mNG pool. For each cell, 2 cytoplasmic measurement points were recorded for 30 seconds per acquisition, with 3 per point. Measurements showing abrupt intensity

fluctuations due to cell movement, passage of large fluorescent structures, photobleaching, or unstable baseline fluorescence were excluded from analysis. Fluorescence intensity traces were extracted and fitted using the same model with two diffusion coefficients.

$$G(\tau) = 1 + \frac{1}{N}\left(1 + \frac{T}{1-T}e^{\frac{-\tau}{\tau_T}}\right)\sum_{i=1}^{2} a_i \left(1 + \frac{\tau}{\tau_{D_i}}\right)^{-1}\left(1 + \frac{\tau}{\kappa^2\tau_{D_i}}\right)^{-1/2}$$

$a_1 + a_2 = 1$ (relative population of two fluorescent species)

$\tau_{di}$ - diffusion times of the two components

The intracellular concentration of MyD88–mNG was calculated from the fitted molecule number $N$and the calibrated effective confocal volume $V_{\text{eff}}$according to

$$C = \frac{N}{N_A V_{\text{eff}}}$$

where $N_A$is Avogadro's number. Concentrations were reported as local cytoplasmic MyD88-mNG concentration per cell. The final result is pooled from 25 cells across 3 independent biological replicates. Cells with poor fluorescence signal, saturated pixels, excessive photobleaching, abnormal morphology, or poor autocorrelation fits were excluded using the same criteria across all conditions. An important approximation for the concentration measurement was considering an uniform distribution of MyD88 mNG throughout the cell (except the nucleus), which is valid for an unstimulated cell.

**Approximate estimation of MyD88 molecules per cell**

To estimate the number of MyD88 molecules per cell, we first calculated the approximate cellular volume from confocal z-stack images. The perimeter of individual cells was measured in Fiji/ImageJ, and the projected cell area was estimated using a circular approximation, where the cell radius was calculated from the measured perimeter. Cell height was estimated from the number of acquired z-slices multiplied by the z-step size of 0.5 µm. The volume of each cell was then calculated as the product of the projected area and estimated height. Based on this approach, cellular volumes ranged from approximately 3 to 15 pL. The number of MyD88 molecules per cell was then estimated from the FCS-derived MyD88 concentration range of 7–92 nM using Avogadro's constant. This yielded an estimated range of approximately 12,600 to 831,500 MyD88 molecules per cell.

**Immunocytochemistry (general protocol followed)**

- Cells were seeded on glass-bottom dishes or imaging chambers and allowed to adhere overnight before stimulation.
- Cells were stimulated with the indicated ligands for the required dosage and time points and then fixed 50 mg/ml dimethyl pimelimidate (DMP: ThermoFisher Scientific; Catalog number: 21667) or with 4% paraformaldehyde in PBS for 15 mins at room temperature.

- After fixation, cells were washed with PBS and permeabilized with 0.1% Triton X-100 in PBS for 5 mins.
- Non-specific binding was blocked using 3 % BSA, in PBS for 60 min at room temperature. Purified rabbit anti-mouse CD16/CD32 (BD Pharmingen™, Catalog number: 567021) was supplemented to the blocking solution at a concentration of 4 µg/ml.
- Cells were incubated with the indicated primary antibodies diluted in 1% BSA (in PBS buffer) either overnight at 4°C or for 3 h at room temperature.
- After washing, cells were incubated with specific secondary antibodies of required dilution for 45 mins at room temperature in the dark.
- Nuclei were counterstained with DAPI depending on experimental requirements.
- For quantitative comparison, all samples were processed using identical staining conditions and imaged using matched microscope settings.

**Measurement of cell-to-cell MyD88 heterogeneity by immunocytochemistry**

For intensity-based measurement of MyD88 heterogeneity, MyD88–mNG iBMDMs, WT iBMDMs, and primary BMDMs were plated in ibidi 8-well high imaging chambers at a density of $0.3 \times 10^6$ cells and allowed to adhere overnight. Cells were fixed and permeabilized according to the general immunocytochemistry procedure described above. MyD88 was labelled using an anti-mouse MyD88 antibody raised in goat (R&D Systems, AF3109), diluted in 1% BSA to a final concentration of 2.5 µg/mL, and incubated with cells for 3 h at room temperature. After washing, cells were incubated with Alexa Fluor 647-conjugated donkey anti-goat IgG secondary antibody at 1:1000 dilution for 45 min at room temperature. Samples were washed and imaged under identical acquisition settings for quantitative comparison of MyD88 intensity across cells and cell types.

**Longitudinal measurement of MyD88 heterogeneity during cell division**

To determine how MyD88-mNG heterogeneity is maintained during cell division, MyD88-mNG iBMDMs were seeded at low density on micropatterned ibidi imaging chambers containing circular adhesive regions separated by bioinert areas (µ-Slide 8 Well high µ-Pattern ibiTreat, cir200, pit600, hex; catalog no. 83812). At this seeding density, most wells were empty, while a subset contained one or two cells at the start of imaging. The patterned wells restricted cell growth within the adhesive regions and prevented migration outside the wells, thereby minimizing migration-induced artifacts during longitudinal measurements. Weak fluorescence from the bioinert ibidi coating upon 488 nm excitation enabled repeated identification and imaging of the same wells over time. The wells themselves showed negligible background fluorescence; therefore, no background subtraction was applied. Cells were plated and imaged after 4 hrs in FluoroBrite complete DMEM using spinning-disk confocal microscopy. From day 2 onward, imaging was performed at 24 h intervals until

individual wells reached confluency. After each imaging session, the medium was replaced with fresh medium, and cells were returned to 37°C to allow continued growth and division.

For each time point, confocal z-stacks were converted into sum-intensity projections before quantification. Integrated MyD88-mNG fluorescence intensity was measured from individual cell regions of interest within each identified well and used as an estimate of total cellular MyD88-mNG abundance. MyD88-mNG heterogeneity was quantified as the coefficient of variation (%CV) of integrated cellular MyD88-mNG intensity:

$$\%CV = (\text{standard deviation} / \text{mean}) \times 100$$

This longitudinal approach enabled repeated measurement of MyD88-mNG intensity heterogeneity in the same confined cell populations during colony growth.

**Cell-cycle phase measurement using Vybrant Dyecycle Ruby**

Cell-cycle phase of MyD88–mNeonGreen cells was assessed using Vybrant DyeCycle Ruby stain (Invitrogen, V10309). Cells were incubated with 5 µM Vybrant DyeCycle Ruby in pre-warmed medium for 10 min at 37°C protected from light and imaged live immediately after staining. MyD88–mNG and Vybrant DyeCycle Ruby were detected in the green and far-red channels, respectively. Nuclei were segmented using the Ruby channel, and integrated nuclear Ruby fluorescence intensity was used as a measure of DNA content. Cells were classified into G0/G1, and G2/M phases based on the peak intensities (2N and 4N DNA-content distributions) respectively. Identical staining, imaging, and analysis settings were used across conditions.

To assign cells to distinct DNA-content states, a probabilistic classification approach was used. For each cell, the integrated nuclear DyeCycle Ruby intensity was measured as a proxy for DNA content, together with the corresponding whole-cell MyD88–mNG intensity. The distribution of DyeCycle Ruby intensities across all cells was fitted with a sum of two Gaussian functions, representing two major DNA-content populations. For each cell, the probability of belonging to either Gaussian population was estimated from the relative contribution of each fitted Gaussian at that cell's DyeCycle Ruby intensity. Specifically, the value of each Gaussian component at a given DyeCycle intensity was divided by the value of the total two-Gaussian fit at the same intensity. This yielded the probability that the cell belonged to population 1 or population 2. Cells were assigned to a given DNA-content population only if the probability of belonging to that population was greater than 0.8. Cells that did not meet this probability threshold were excluded from phase-specific comparison. The MyD88–mNG intensities of cells assigned to each population were then used to generate and compare the corresponding MyD88 intensity distributions.

**Measurement of phosphorylated p65 in MyD88-mNG cells using Immunochemistry**

Phospho-p65 immunocytochemistry was performed using the general immunocytochemistry procedure described above. During stimulation with LPS or MPLA, Roche PhosSTOP phosphatase inhibitor cocktail was added to the stimulation medium at 1:10 dilution. (the

PhosSTOP stock was prepared by dissolving one tablet in 1 mL PBS). After stimulation, cells were fixed, permeabilized, and blocked as described above. Phospho-NFκB p65 was labelled using an Alexa Fluor 647-conjugated primary antibody against phospho-NFκB p65 Ser536 (93H1, Cell Signaling Technology), diluted 1:50 in 1% BSA. Cells were incubated with the antibody overnight at 4°C. The following day, samples were washed, nucleus stained with DAPI, and imaged. MyD88–mNG fluorescence was detected directly in the green channel, Phospho-p65 in far red, and DAPI in 405 channel.

**Single cell TNFα imaging**

Single-cell TNFα expression was measured using two complementary strategies. In the first approach, MyD88–mNeonGreen cells were seeded in ibidi 8-well high imaging chambers at a density of $0.3 \times 10^6$ cells per well and allowed to adhere overnight. The following day, the media was replaced with LPS or MPLA containing media supplemented with 1 µM TAPI-0 (Merck, 579050), and cells were stimulated for 4 h at 37°C and 5% $CO_2$. Before stimulation, the LPS stock solution (1 mg/mL) was sonicated for 1 min. To inhibit TLR4 signaling, TAK-242 (Merck, 614316) was added at a final concentration of 2 µM at the indicated time points. After 4 h of stimulation, cells were washed with ice-cold PBS containing 1 µM TAPI-0 and fixed with 2% PFA for 20 min at 4°C. Cells were then blocked with 3% BSA supplemented with 4 µg/mL rat anti-mouse CD16/32 for 2 h at room temperature. TNFα was labelled by incubating cells overnight at 4°C with Alexa Fluor 647-conjugated rat anti-mouse TNFα antibody (BioLegend, clone MP6-XT22, Cat. 506314) at a final concentration of 10 µg/mL.

For the second strategy, MyD88 assembly formation and intracellular TNFα accumulation were measured simultaneously after 4 h of stimulation. To retain TNFα intracellularly, Brefeldin A 1000X solution was used (Thermo Fisher Scientific, Cat. 00-4506-51). Briefly, primary BMDMs and MyD88–mNG cells were seeded in ibidi 8-well high imaging chambers at a density of $0.3 \times 10^6$ cells per well and allowed to adhere overnight. Primary BMDMs were cultured according to the procedure described above. The following day, the media was replaced with LPS-containing media. After 2 h of stimulation, Brefeldin A was added to the media at a final concentration of 2 µg/mL to inhibit protein transport through the Golgi pathway and retain newly synthesized TNFα intracellularly (in the ER). Cells were fixed after a total stimulation period of 4 h and permeabilized using the standard immunocytochemistry procedure described above, including DMP and Triton X-100 treatment. MyD88 assemblies and intracellular TNFα were then detected using the staining and imaging procedures described above.

**Measurement of A20 in MyD88-mNG cells using Immunochemistry**

A20/TNFAIP3 expression was detected by immunocytochemistry following 4 h stimulation with LPS or MPLA. Briefly, MyD88–mNG cells were stimulated under the indicated conditions, fixed, permeabilized, and blocked using the standard immunocytochemistry procedure described above. A20 was labelled using an A20/TNFAIP3-specific rabbit monoclonal primary

antibody (Cell Signaling Technology, D13H3), diluted in 1% BSA (1:100), and incubated with the cells overnight at 4°C. After washing, cells were incubated with Alexa Fluor 555-conjugated goat anti-rabbit IgG Fc secondary antibody (Abcam, ab150078) at 1:1000 dilution for 45 mins at room temperature in the dark. Samples were washed and imaged using the Alexa Fluor 555 channel, while endogenous MyD88–mNeonGreen fluorescence was detected directly in the green channel.

**3D reconstruction of cell body, MyD88 assembly, and comparative estimation of phosphor-p65 nuclear translocation in MyD88 mNG cells**

Three-dimensional reconstruction and image analysis were performed in Imaris microscopy image analysis software (Oxford instruments) using confocal z-stack images. Cell bodies were reconstructed using the Surfaces function from the cell surface/cell body channel and used as masks for single-cell analysis. Nuclei were segmented from the DAPI channel using the Surfaces module. For each DAPI-defined nuclear surface, the mean phospho-p65 fluorescence intensity was measured within the nuclear volume and used to colour-code nuclei according to nuclear phospho-p65 content. MyD88–mNG puncta were detected from the mNG channel using the Spots function, with spot diameter and quality/intensity thresholds kept constant across comparable images. Spots outside reconstructed cell surfaces were excluded, and puncta number, puncta intensity, and puncta position were extracted on a per-cell basis. Cells or nuclei with poor segmentation, saturated signal, incomplete boundaries, or imaging artefacts were excluded from analysis.

**BulkRNAseq differential expression analysis from ROSMAP cohort**

BulkRNAseq data from the Religious Orders Study and Memory and Aging Project (ROSMAP) dorsolateral prefrontal cortex (DLPFC) cohort were analysed using DESeq2 (v1.x). The RSEM FPKM gene level data along with the sample level metadata were downloaded from https://www.synapse.org/Synapse:syn3219045. Sample metadata were supplemented with microglial morphological fraction scores (mglia3_mf, mglia123_mf) derived from published neuropathological assessments[77]. Continuous covariates — age at death, post-mortem interval (PMI), RNA integrity number (RIN), tissue amyloid burden (square-root transformed), tissue tangle burden (square-root transformed), and microglial fraction scores — were z-score standardised prior to modelling.

Variance-stabilising transformation (VST) was applied to the normalised count matrix (blind = FALSE) for visualisation purposes. Differential expression was performed separately for each dependent variable of interest: Braak stage (continuous, scaled), amyloid burden (sqrt.amyloid) and tau burden (sqrt.tangles). For each model, the design formula included the dependent variable of interest alongside the following covariates: RIN, sex, age at death, APOE genotype group, and sequencing library batch. Size factors were re-estimated and DESeq2's Wald test was applied.

**Single-nucleus RNAseq Pseudobulk Analysis (Microglia)**

Transcriptomic data on microglia were downloaded as a pre-processed Seurat object from the ROSMAP DLPFC single-nucleus RNAseq dataset from https://www.synapse.org/Synapse:syn3219045. Raw counts were aggregated per donor (pseudobulk) by summing counts across all microglial nuclei assigned to each individual using the individualID field. Donor-level metadata including Braak stage, diagnosis, age at death, sex, APOE genotype, amyloid burden and tau burden were retained. A DESeqDataSet was constructed from the pseudobulk count matrix and donor metadata. Size factors were estimated and VST was applied for normalisation. Visualisation of gene expression was performed on the VST-transformed pseudobulk matrix.

**Visualisation**

For both bulk and pseudobulk datasets, VST-transformed expression values for genes of interest were visualised as a function of Braak stage using overlaid jitter plots with mean ± standard error of the mean (SEM) trend lines. One-way ANOVA p-values were computed per gene across Braak stages using stat_compare_means from the ggpubr package. Continuous pathological burden variables (amyloid, tangles and mglia123_mf) were plotted against gene expression using LOESS smoothing curves with Pearson correlation coefficients computed via stat_cor. A dot plot of microglial gene expression stratified by diagnosis (Control, Braak < 3; AD, Braak ≥ 3) was generated using Seurat's DotPlot function. All plots were produced using ggplot2.

**Transcriptomic analysis of publicly available human disease datasets**

Differential gene expression was assessed across publicly available datasets (GEO accessions GSE186507, GSE161731, and GSE154918), using analysis methods matched to each dataset's underlying data type. For the Mount Sinai IBD cohort (GSE186507; whole-blood RNA-seq) Crohn's disease (n = 432), and ulcerative colitis (n = 389) were each compared against healthy controls (n = 209) using the covariate-adjusted, log2-scale expression matrix provided by the study authors. Because these values were already continuous and adjusted rather than raw counts, differential expression was assessed with a per-gene Welch's t-test (unequal variance, two-sided) rather than a count-based model. For the Duke respiratory infection cohort (GSE161731; whole-blood RNA-seq), influenza (n = 17) and SARS-CoV-2/COVID-19 (n = 77, PCR-confirmed, distinct from a separate non-SARS-CoV-2 "other coronavirus" group) were each compared against healthy controls (n = 19) using DESeq2's negative binomial generalized linear model (implemented via pydeseq2 v0.5.4), with size-factor normalization, dispersion estimation, and Wald testing performed per DESeq2's standard workflow. For the Schughart sepsis cohort (GSE154918; whole-blood, pre-normalized log2 expression, n = 105), sepsis (n = 20), and septic shock (n = 19) were each compared against healthy controls (Healthy, n = 40) using limma (R/Bioconductor v3.58.1): a single linear model was fit jointly across all four

groups (~status, healthy as reference), followed by empirical Bayes moderation (eBayes) to obtain a shared, better-powered variance estimate across contrasts. Across all analyses, raw p-values were adjusted for multiple testing using the Benjamini–Hochberg procedure to control the false discovery rate, and genes were considered significantly differentially expressed at an adjusted p-value (padj) < 0.05 combined with a fold-change cutoff (|log2FC| > 1, or > 0.5 for the GSE186507 comparisons). For MCI[78], PD[79], ALS[80], and SCI[81], differential expression values of genes (w.r.t to control) were available as extended information tables in the respective manuscripts. Cohort metadata is added in the following table.

| Disease | Disease Category | RNA-seq material | Disease (n) | Control (n) | Age-group (yrs) |
|---|---|---|---|---|---|
| MCI | Chronic neurodegenerative / cognitive impairment | PBMCs; single-cell CITE-seq, with monocyte-specific DE | 20 | 20 | 55.8 ± 6 |
| PD | Chronic neurodegenerative | PAXgene whole blood; bulk RNA-seq | 423 | 196 | 55-65 |
| ALS | Chronic neurodegenerative | PAXgene whole blood; bulk RNA-seq | 121 | 53 | 59.8 ± 10 |
| CD | Chronic inflammatory bowel disease | Whole blood; bulk RNA-seq | 432 | 209 | 19-76 |
| UC | Chronic inflammatory bowel disease | Whole blood; bulk RNA-seq | 389 | 209 | 20-82 |
| Influenza | Acute viral respiratory infection | PAXgene whole blood; bulk RNA-seq | 17 | 19 | 14-51 |
| Acute SCI | Acute sterile inflammation following traumatic CNS injury | Peripheral white blood cells / circulating leukocytes; bulk RNA-seq | 38 | 10 | 55.3 ± 20 |
| Covid 19 | Acute viral respiratory infection | PAXgene whole blood; bulk RNA-seq | 46 | 19 | 20-91 |
| Sepsis | Acute systemic infection-associated inflammation | PAXgene whole blood; bulk RNA-seq | 20 | 40 | Adults ≥18 years |
| Septic Shock | Acute severe systemic infection with circulatory/organ dysfunction | PAXgene whole blood; bulk RNA-seq | 19 | 40 | Adults ≥18 years |

For each dataset, we obtained gene-level log2 fold changes and $P$-values for the comparison between patients and the corresponding control group. To incorporate both the direction and statistical strength of differential expression, we calculated a signed Z-score for each gene:

$$Z_i = sign(log_2 FC_i)\Phi^{-1}(1 - \frac{p_i}{2})$$

where $\Phi^{-1}$denotes the inverse cumulative distribution function of the standard normal distribution and $p_i$denotes the [raw/adjusted] two-sided $P$-value for gene $i$.

The effective sample size for each case–control comparison was calculated as:

$$n_{eff} = \frac{n_{case} \times n_{control}}{n_{case} + n_{control}}$$

To scale the Z-scores to the effective sample size of the smallest cohort, we calculated:

$$Z_{i-scaled} = Z_i \times \sqrt{\frac{n_{eff(small)}}{n_{eff(i)}}}$$

Prespecified inflammatory and feedback-regulatory scores were calculated as the arithmetic means of the available scaled signed Z-scores. The inflammatory genes comprised [NFKBIZ, NFKBIA, TLR2, TLR4, TLR9, ICAM1, IL1B, and PTGS2], whereas the feedback-regulatory module comprised [TNFAIP3, SOCS1, SOCS3 and ZC3H12A]. Notably, as seen from our in-vitro data, NFKBIA expression did not correlate with extent of agonism, hence it was included in the inflammatory module as a measure of proximal NF-κB activation.

For each cohort, we then calculated the difference between the inflammatory and feedback-regulatory scores as

$$\Delta Z_{cohort} = Z_{inflammatory} - Z_{feedback}$$

Where, a positive value indicates weaker feedback-regulatory engagement, and a negative value indicates equal or stronger engagement of feedback-regulatory genes.

**Statistical analysis**

Statistical analyses were performed using OriginLab and GraphPad Prism. Data are presented as mean ± SE, mean± SD, or full single-cell distributions as indicated in the figure legends. For comparisons between two groups, unpaired, two-tailed Student's *t* test was used. For multiple comparisons, Kruskal-Wallis ANOVA was used. For comparison of single cell distributions, Kolmogorov-Smirnov (KS) nonparametric test was performed. Biological replicates refer to independent cell culture experiments performed on different days. Technical replicates refer to repeated wells or fields of view within the same experiment. The number of cells, fields of view, and biological replicates analyzed for each experiment are indicated in the corresponding figure legends. A *$p$ or adjusted *$p$ value of <0.05 was considered statistically significant unless otherwise specified.

**References**

1. Fullerton, J.N., and Gilroy, D.W. (2016). Resolution of inflammation: a new therapeutic frontier. Nat Rev Drug Discov *15*, 551–567. https://doi.org/10.1038/nrd.2016.39.

2. Serhan, C.N., and Savill, J. (2005). Resolution of inflammation: the beginning programs the end. Nat Immunol *6*, 1191–1197. https://doi.org/10.1038/ni1276.

3. Lawrence, T., and Gilroy, D.W. (2007). Chronic inflammation: a failure of resolution? Int J Experimental Path *88*, 85–94. https://doi.org/10.1111/j.1365-2613.2006.00507.x.

4. Sato, S., Sugiyama, M., Yamamoto, M., Watanabe, Y., Kawai, T., Takeda, K., and Akira, S. (2003). Toll/IL-1 Receptor Domain-Containing Adaptor Inducing IFN-β (TRIF) Associates with TNF Receptor-Associated Factor 6 and TANK-Binding Kinase 1, and Activates Two Distinct Transcription Factors, NF-κB and IFN-Regulatory Factor-3, in the Toll-Like Receptor Signaling. The Journal of Immunology *171*, 4304–4310. https://doi.org/10.4049/jimmunol.171.8.4304.

5. Kawasaki, T., and Kawai, T. (2014). Toll-Like Receptor Signaling Pathways. Front. Immunol. *5*. https://doi.org/10.3389/fimmu.2014.00461.

6. Kawai, T., and Akira, S. (2007). Signaling to NF-κB by Toll-like receptors. Trends in Molecular Medicine *13*, 460–469. https://doi.org/10.1016/j.molmed.2007.09.002.

7. Fisch, D., Zhang, T., Sun, H., Ma, W., Tan, Y., Gygi, S.P., Higgins, D.E., and Kagan, J.C. (2024). Molecular definition of the endogenous Toll-like receptor signalling pathways. Nature *631*, 635–644. https://doi.org/10.1038/s41586-024-07614-7.

8. Moncrieffe, M.C., Suresh, P., Boyle, J., Cui, Y., Nawalpuri, B., Verstak, B., Zhang, Y.P., Zhang, Z., Taylor, M., Egelman, E.H., et al. (2026). Toll-like receptor signaling outcome is determined by the stoichiometry of the endogenous TRIFosome. Sci. Adv. *12*, eaeb9507. https://doi.org/10.1126/sciadv.aeb9507.

9. Deliz-Aguirre, R., Cao, F., Gerpott, F.H.U., Auevechanichkul, N., Chupanova, M., Mun, Y., Ziska, E., and Taylor, M.J. (2021). MyD88 oligomer size functions as a physical threshold to trigger IL1R Myddosome signaling. Journal of Cell Biology *220*, e202012071. https://doi.org/10.1083/jcb.202012071.

10. Latty, S.L., Sakai, J., Hopkins, L., Verstak, B., Paramo, T., Berglund, N.A., Cammarota, E., Cicuta, P., Gay, N.J., Bond, P.J., et al. (2018). Activation of Toll-like receptors nucleates assembly of the MyDDosome signaling hub. eLife *7*, e31377. https://doi.org/10.7554/eLife.31377.

11. Tay, S., Hughey, J.J., Lee, T.K., Lipniacki, T., Quake, S.R., and Covert, M.W. (2010). Single-cell NF-κB dynamics reveal digital activation and analogue information processing. Nature *466*, 267–271. https://doi.org/10.1038/nature09145.

12. Cheng, Z., Taylor, B., Ourthiague, D.R., and Hoffmann, A. (2015). Distinct single-cell signaling characteristics are conferred by the MyD88 and TRIF pathways during TLR4 activation. Sci. Signal. *8*. https://doi.org/10.1126/scisignal.aaa5208.

13. Mata-Haro, V., Cekic, C., Martin, M., Chilton, P.M., Casella, C.R., and Mitchell, T.C. (2007). The Vaccine Adjuvant Monophosphoryl Lipid A as a TRIF-Biased Agonist of TLR4. Science *316*, 1628–1632. https://doi.org/10.1126/science.1138963.

14. Jin, M.S., Kim, S.E., Heo, J.Y., Lee, M.E., Kim, H.M., Paik, S.-G., Lee, H., and Lee, J.-O. (2007). Crystal Structure of the TLR1-TLR2 Heterodimer Induced by Binding of a Tri-Acylated Lipopeptide. Cell *130*, 1071–1082. https://doi.org/10.1016/j.cell.2007.09.008.

15. Lin, S.-C., Lo, Y.-C., and Wu, H. (2010). Helical assembly in the MyD88–IRAK4–IRAK2 complex in TLR/IL-1R signalling. Nature *465*, 885–890. https://doi.org/10.1038/nature09121.

16. Moncrieffe, M.C., Bollschweiler, D., Li, B., Penczek, P.A., Hopkins, L., Bryant, C.E., Klenerman, D., and Gay, N.J. (2020). MyD88 Death-Domain Oligomerization Determines Myddosome Architecture: Implications for Toll-like Receptor Signaling. Structure *28*, 281-289.e3. https://doi.org/10.1016/j.str.2020.01.003.

17. Park, B.S., Song, D.H., Kim, H.M., Choi, B.-S., Lee, H., and Lee, J.-O. (2009). The structural basis of lipopolysaccharide recognition by the TLR4–MD-2 complex. Nature *458*, 1191–1195. https://doi.org/10.1038/nature07830.

18. Tanimura, N., Saitoh, S., Ohto, U., Akashi-Takamura, S., Fujimoto, Y., Fukase, K., Shimizu, T., and Miyake, K. (2014). The attenuated inflammation of MPL is due to the lack of CD14-dependent tight dimerization of the TLR4/MD2 complex at the plasma membrane. International Immunology *26*, 307–314. https://doi.org/10.1093/intimm/dxt071.

19. Fu, Y., Kim, H., Lee, D.S., Han, A., Heine, H., Zamyatina, A., and Kim, H.M. (2025). Structural insight into TLR4/MD-2 activation by synthetic LPS mimetics with distinct binding modes. Nat Commun *16*, 4164. https://doi.org/10.1038/s41467-025-59550-3.

20. Kagan, J.C., Su, T., Horng, T., Chow, A., Akira, S., and Medzhitov, R. (2008). TRAM couples endocytosis of Toll-like receptor 4 to the induction of interferon-β. Nat Immunol *9*, 361–368. https://doi.org/10.1038/ni1569.

21. O'Carroll, A., Chauvin, B., Brown, J.W.P., Meagher, A., Coyle, J., Schill, J., Bhumkhar, A., Hunter, D.J.B., Ve, T., Kobe, B., et al. (2018). Pathological mutations differentially affect the self-assembly and polymerisation of the innate immune system signalling adaptor molecule MyD88. BMC Biol *16*, 149. https://doi.org/10.1186/s12915-018-0611-7.

22. Wu, H. (2013). Higher-Order Assemblies in a New Paradigm of Signal Transduction. Cell *153*, 287–292. https://doi.org/10.1016/j.cell.2013.03.013.

23. Haupts, U., Maiti, S., Schwille, P., and Webb, W.W. (1998). Dynamics of fluorescence fluctuations in green fluorescent protein observed by fluorescence correlation spectroscopy. Proc. Natl. Acad. Sci. U.S.A. *95*, 13573–13578. https://doi.org/10.1073/pnas.95.23.13573.

24. Zhang, L., Perez-Romero, C., Dostatni, N., and Fradin, C. (2021). Using FCS to accurately measure protein concentration in the presence of noise and

photobleaching. Biophysical Journal *120*, 4230–4241. https://doi.org/10.1016/j.bpj.2021.06.035.

25. Ohto, U., Fukase, K., Miyake, K., and Shimizu, T. (2012). Structural basis of species-specific endotoxin sensing by innate immune receptor TLR4/MD-2. Proc. Natl. Acad. Sci. U.S.A. *109*, 7421–7426. https://doi.org/10.1073/pnas.1201193109.

26. Hussain, S., Johnson, C.G., Sciurba, J., Meng, X., Stober, V.P., Liu, C., Cyphert-Daly, J.M., Bulek, K., Qian, W., Solis, A., et al. (2020). TLR5 participates in the TLR4 receptor complex and promotes MyD88-dependent signaling in environmental lung injury. eLife *9*, e50458. https://doi.org/10.7554/eLife.50458.

27. Ferrao, R., Li, J., Bergamin, E., and Wu, H. (2012). Structural Insights into the Assembly of Large Oligomeric Signalosomes in the Toll-Like Receptor–Interleukin-1 Receptor Superfamily. Sci. Signal. *5*. https://doi.org/10.1126/scisignal.2003124.

28. Smale, S.T. (2010). Selective Transcription in Response to an Inflammatory Stimulus. Cell *140*, 833–844. https://doi.org/10.1016/j.cell.2010.01.037.

29. Hochrainer, K., Racchumi, G., and Anrather, J. (2013). Site-specific Phosphorylation of the p65 Protein Subunit Mediates Selective Gene Expression by Differential NF-κB and RNA Polymerase II Promoter Recruitment. Journal of Biological Chemistry *288*, 285–293. https://doi.org/10.1074/jbc.M112.385625.

30. Bagaev, A.V., Garaeva, A.Y., Lebedeva, E.S., Pichugin, A.V., Ataullakhanov, R.I., and Ataullakhanov, F.I. (2019). Elevated pre-activation basal level of nuclear NF-κB in native macrophages accelerates LPS-induced translocation of cytosolic NF-κB into the cell nucleus. Sci Rep *9*, 4563. https://doi.org/10.1038/s41598-018-36052-5.

31. Sakai, J., Cammarota, E., Wright, J.A., Cicuta, P., Gottschalk, R.A., Li, N., Fraser, I.D.C., and Bryant, C.E. (2017). Lipopolysaccharide-induced NF-κB nuclear translocation is primarily dependent on MyD88, but TNFα expression requires TRIF and MyD88. Sci Rep *7*, 1428. https://doi.org/10.1038/s41598-017-01600-y.

32. Reynoso, M., Hobbs, S., Kolb, A.L., Matheny, R.W., and Roberts, B.M. (2023). MyD88 and not TRIF knockout is sufficient to abolish LPS-induced inflammatory responses in bone-derived macrophages. FEBS Letters *597*, 1225–1232. https://doi.org/10.1002/1873-3468.14616.

33. Singh, A., Sen, S., Iter, M., Adelaja, A., Luecke, S., Guo, X., and Hoffmann, A. (2024). Stimulus-response signaling dynamics characterize macrophage polarization states. Cell Systems *15*, 563-577.e6. https://doi.org/10.1016/j.cels.2024.05.002.

34. Hoffmann, A., Levchenko, A., Scott, M.L., and Baltimore, D. (2002). The IκB-NF-κB Signaling Module: Temporal Control and Selective Gene Activation. Science *298*, 1241–1245. https://doi.org/10.1126/science.1071914.

35. Hobbs, S., Reynoso, M., Geddis, A.V., Mitrophanov, A.Y., and Matheny, R.W. (2018). LPS-stimulated NF-κB p65 dynamic response marks the initiation of TNF

expression and transition to IL-10 expression in RAW 264.7 macrophages. Physiol Rep *6*, e13914. https://doi.org/10.14814/phy2.13914.

36. Rosadini, C.V., Zanoni, I., Odendall, C., Green, E.R., Paczosa, M.K., Philip, N.H., Brodsky, I.E., Mecsas, J., and Kagan, J.C. (2015). A Single Bacterial Immune Evasion Strategy Dismantles Both MyD88 and TRIF Signaling Pathways Downstream of TLR4. Cell Host & Microbe *18*, 682–693. https://doi.org/10.1016/j.chom.2015.11.006.

37. Kondo, T., Kawai, T., and Akira, S. (2012). Dissecting negative regulation of Toll-like receptor signaling. Trends in Immunology *33*, 449–458. https://doi.org/10.1016/j.it.2012.05.002.

38. Lee, F.F.Y., and Alper, S. (2022). Alternative pre-mRNA splicing as a mechanism for terminating Toll-like Receptor signaling. Front. Immunol. *13*, 1023567. https://doi.org/10.3389/fimmu.2022.1023567.

39. Pustelny, K., Kuska, K., Gorecki, A., Musielak, B., Dobosz, E., Wladyka, B., Koziel, J., Czarna, A., Holak, T., and Dubin, G. (2022). Mechanism of MyD88S mediated signal termination. Cell Commun Signal *20*, 10. https://doi.org/10.1186/s12964-021-00811-1.

40. Hamerman, J.A., Pottle, J., Ni, M., He, Y., Zhang, Z., and Buckner, J.H. (2016). Negative regulation of TLR signaling in myeloid cells—implications for autoimmune diseases. Immunological Reviews *269*, 212–227. https://doi.org/10.1111/imr.12381.

41. Fujita, M., Gao, Z., Zeng, L., McCabe, C., White, C.C., Ng, B., Green, G.S., Rozenblatt-Rosen, O., Phillips, D., Amir-Zilberstein, L., et al. (2024). Cell subtype-specific effects of genetic variation in the Alzheimer's disease brain. Nat Genet *56*, 605–614. https://doi.org/10.1038/s41588-024-01685-y.

42. Burns, K., Janssens, S., Brissoni, B., Olivos, N., Beyaert, R., and Tschopp, J. (2003). Inhibition of interleukin 1 receptor/Toll-like receptor signaling through the alternatively spliced, short form of MyD88 is due to its failure to recruit IRAK-4. J Exp Med *197*, 263–268. https://doi.org/10.1084/jem.20021790.

43. Vereecke, L., Beyaert, R., and Van Loo, G. (2009). The ubiquitin-editing enzyme A20 (TNFAIP3) is a central regulator of immunopathology. Trends in Immunology *30*, 383–391. https://doi.org/10.1016/j.it.2009.05.007.

44. Croker, B.A., Kiu, H., and Nicholson, S.E. (2008). SOCS regulation of the JAK/STAT signalling pathway. Semin Cell Dev Biol *19*, 414–422. https://doi.org/10.1016/j.semcdb.2008.07.010.

45. Lang, R., Hammer, M., and Mages, J. (2006). DUSP Meet Immunology: Dual Specificity MAPK Phosphatases in Control of the Inflammatory Response. The Journal of Immunology *177*, 7497–7504. https://doi.org/10.4049/jimmunol.177.11.7497.

46. Matsushita, K., Takeuchi, O., Standley, D.M., Kumagai, Y., Kawagoe, T., Miyake, T., Satoh, T., Kato, H., Tsujimura, T., Nakamura, H., et al. (2009). Zc3h12a is an RNase

essential for controlling immune responses by regulating mRNA decay. Nature *458*, 1185–1190. https://doi.org/10.1038/nature07924.

47. Kaltschmidt, B., Uherek, M., Volk, B., Baeuerle, P.A., and Kaltschmidt, C. (1997). Transcription factor NF-κB is activated in primary neurons by amyloid β peptides and in neurons surrounding early plaques from patients with Alzheimer disease. Proc. Natl. Acad. Sci. U.S.A. *94*, 2642–2647. https://doi.org/10.1073/pnas.94.6.2642.

48. Hartman, Z.C., Osada, T., Glass, O., Yang, X.Y., Lei, G., Lyerly, H.K., and Clay, T.M. (2010). Ligand-Independent Toll-like Receptor Signals Generated by Ectopic Overexpression of MyD88 Generate Local and Systemic Antitumor Immunity. Cancer Research *70*, 7209–7220. https://doi.org/10.1158/0008-5472.CAN-10-0905.

49. Lee, A.-J., Cho, K.-J., and Kim, J.-H. (2015). MyD88–BLT2-dependent cascade contributes to LPS-induced interleukin-6 production in mouse macrophage. Exp Mol Med *47*, e156–e156. https://doi.org/10.1038/emm.2015.8.

50. Da Silva, R.A.G., Tien, B.Y.Q., Kao, P.H.N., Antypas, H., Celik, C., Tan, A.Z.C., Ismail, M.H., Hu, G., Chong, K.K.L., Thibault, G., et al. (2026). Enterococcus faecalis-derived lactic acid suppresses macrophage activation to facilitate persistent and polymicrobial wound infections. Cell Host & Microbe *34*, 245-262.e8. https://doi.org/10.1016/j.chom.2026.01.002.

51. Rodriguez Gama, A., Miller, T., Lange, J.J., Unruh, J.R., and Halfmann, R. (2022). A nucleation barrier spring-loads the CBM signalosome for binary activation. eLife *11*, e79826. https://doi.org/10.7554/eLife.79826.

52. Rodriguez Gama, A., Miller, T., Venkatesan, S., Lange, J.J., Wu, J., Song, X., Bradford, W.D., Cook, M., Unruh, J.R., and Halfmann, R. (2026). Adaptor protein supersaturation drives innate immune signaling and cell fate. eLife *14*, RP107962. https://doi.org/10.7554/eLife.107962.3.

53. Li, B., Suresh, P., Brelstaff, J., Kedia, S., Bryant, C.E., and Klenerman, D. (2024). The delayed kinetics of Myddosome formation explains why amyloid-beta aggregates trigger Toll-like receptor 4 less efficiently than lipopolysaccharide. eLife *13*, RP92350. https://doi.org/10.7554/eLife.92350.3.

54. Castro-Gomez, S., and Heneka, M.T. (2024). Innate immune activation in neurodegenerative diseases. Immunity *57*, 790–814. https://doi.org/10.1016/j.immuni.2024.03.010.

55. Wightman, D.P., Jansen, I.E., Savage, J.E., Shadrin, A.A., Bahrami, S., Holland, D., Rongve, A., Børte, S., Winsvold, B.S., Drange, O.K., et al. (2021). A genome-wide association study with 1,126,563 individuals identifies new risk loci for Alzheimer's disease. Nat Genet *53*, 1276–1282. https://doi.org/10.1038/s41588-021-00921-z.

56. Lu, A., Chen, W.-T., Dalby, M., Sainz Garcia, D., Vanheusden, M., De Vries, L.E., Van Lieshout, V., Martirosyan, A., Craessaerts, K., Moonen, S., et al. (2026). Human

microglial transitions at the Aβ–tau inflection point associate with divergent pathways to dementia and resilience. Nat Med. https://doi.org/10.1038/s41591-026-04393-8.

57. Voet, S., Mc Guire, C., Hagemeyer, N., Martens, A., Schroeder, A., Wieghofer, P., Daems, C., Staszewski, O., Vande Walle, L., Jordao, M.J.C., et al. (2018). A20 critically controls microglia activation and inhibits inflammasome-dependent neuroinflammation. Nat Commun *9*, 2036. https://doi.org/10.1038/s41467-018-04376-5.

58. Zhou, Q., Wang, H., Schwartz, D.M., Stoffels, M., Park, Y.H., Zhang, Y., Yang, D., Demirkaya, E., Takeuchi, M., Tsai, W.L., et al. (2016). Loss-of-function mutations in TNFAIP3 leading to A20 haploinsufficiency cause an early-onset autoinflammatory disease. Nat Genet *48*, 67–73. https://doi.org/10.1038/ng.3459.

59. Perga, S., Martire, S., Montarolo, F., Navone, N.D., Calvo, A., Fuda, G., Marchet, A., Leotta, D., Chiò, A., and Bertolotto, A. (2017). A20 in Multiple Sclerosis and Parkinson's Disease: Clue to a Common Dysregulation of Anti-Inflammatory Pathways? Neurotox Res *32*, 1–7. https://doi.org/10.1007/s12640-017-9724-y.

60. Yan, Z., Yang, W., Parkitny, L., Gibson, S.A., Lee, K.S., Collins, F., Deshane, J.S., Cheng, W., Weinmann, A.S., Wei, H., et al. (2019). Deficiency of Socs3 leads to brain-targeted experimental autoimmune encephalomyelitis via enhanced neutrophil activation and ROS production. JCI Insight *4*, e126520. https://doi.org/10.1172/jci.insight.126520.

61. Iwahara, N., Hisahara, S., Kawamata, J., Matsumura, A., Yokokawa, K., Saito, T., Fujikura, M., Manabe, T., Suzuki, H., Matsushita, T., et al. (2016). Role of Suppressor of Cytokine Signaling 3 (SOCS3) in Altering Activated Microglia Phenotype in APPswe/PS1dE9 Mice. JAD *55*, 1235–1247. https://doi.org/10.3233/JAD-160887.

62. Das, T., Chen, Z., Hendriks, R.W., and Kool, M. (2018). A20/Tumor Necrosis Factor α-Induced Protein 3 in Immune Cells Controls Development of Autoinflammation and Autoimmunity: Lessons from Mouse Models. Front. Immunol. *9*, 104. https://doi.org/10.3389/fimmu.2018.00104.

63. Feng, Y., Chen, Z., Xu, Y., Han, Y., Jia, X., Wang, Z., Zhang, N., and Lv, W. (2023). The central inflammatory regulator IκBζ: induction, regulation and physiological functions. Front. Immunol. *14*, 1188253. https://doi.org/10.3389/fimmu.2023.1188253.

64. Mathes, E., O'Dea, E.L., Hoffmann, A., and Ghosh, G. (2008). NF-κB dictates the degradation pathway of IκBα. EMBO J *27*, 1357–1367. https://doi.org/10.1038/emboj.2008.73.

65. Fletcher, T.C., DiGiandomenico, A., and Hawiger, J. (2010). Extended Anti-inflammatory Action of a Degradation-resistant Mutant of Cell-penetrating Suppressor of Cytokine Signaling 3. Journal of Biological Chemistry *285*, 18727–18736. https://doi.org/10.1074/jbc.M109.095216.

66. Katagiri, C., Masuda, K., Urano, T., Yamashita, K., Araki, Y., Kikuchi, K., and Shima, H. (2005). Phosphorylation of Ser-446 Determines Stability of MKP-7. Journal of Biological Chemistry *280*, 14716–14722. https://doi.org/10.1074/jbc.M500200200.

67. Fazal, F., Dar, N.J., Ahamad, S., Khan, S., Bano, N., Saha, S., Nazir, A., and Bhat, S.A. (2026). cGAS-STING signaling in Alzheimer's disease: Microglial mechanisms and therapeutic opportunities. Molecular Aspects of Medicine *107*, 101444. https://doi.org/10.1016/j.mam.2025.101444.

68. Haney, M.S., Pálovics, R., Munson, C.N., Long, C., Johansson, P.K., Yip, O., Dong, W., Rawat, E., West, E., Schlachetzki, J.C.M., et al. (2024). APOE4/4 is linked to damaging lipid droplets in Alzheimer's disease microglia. Nature *628*, 154–161. https://doi.org/10.1038/s41586-024-07185-7.

69. Carling, G.K., Fan, L., Foxe, N.R., Norman, K., Wong, M.Y., Zhu, D., Corona, C., Razzoli, A., Yu, F., Yarahmady, A., et al. (2024). Alzheimer's disease-linked risk alleles elevate microglial cGAS-associated senescence and neurodegeneration in a tauopathy model. Neuron *112*, 3877-3896.e8. https://doi.org/10.1016/j.neuron.2024.09.006.

70. Lobanova, E., Zhang, Y.P., Emin, D., Brelstaff, J., Kahanawita, L., Malpetti, M., Quaegebeur, A., Triantafilou, K., Triantafilou, M., Zetterberg, H., et al. (2024). ASC specks as a single-molecule fluid biomarker of inflammation in neurodegenerative diseases. Nat Commun *15*, 9690. https://doi.org/10.1038/s41467-024-53547-0.

71. Christoph Gohlke (2026). cgohlke/tifffile: v2026.6.1. Version v2026.6.1 (Zenodo). https://doi.org/10.5281/ZENODO.6795860 https://doi.org/10.5281/ZENODO.6795860.

72. Vincent, L. (1993). Morphological grayscale reconstruction in image analysis: applications and efficient algorithms. IEEE Trans. on Image Process. *2*, 176–201. https://doi.org/10.1109/83.217222.

73. Robinson, K., and Whelan, P.F. (2004). Efficient morphological reconstruction: a downhill filter. Pattern Recognition Letters *25*, 1759–1767. https://doi.org/10.1016/j.patrec.2004.07.002.

74. Lindeberg, T. (1993). Detecting salient blob-like image structures and their scales with a scale-space primal sketch: A method for focus-of-attention. Int J Comput Vision *11*, 283–318. https://doi.org/10.1007/BF01469346.

75. Van Der Walt, S., Schönberger, J.L., Nunez-Iglesias, J., Boulogne, F., Warner, J.D., Yager, N., Gouillart, E., and Yu, T. (2014). scikit-image: image processing in Python. PeerJ *2*, e453. https://doi.org/10.7717/peerj.453.

76. Crocker, J.C., and Grier, D.G. (1996). Methods of Digital Video Microscopy for Colloidal Studies. Journal of Colloid and Interface Science *179*, 298–310. https://doi.org/10.1006/jcis.1996.0217.

77. Felsky, D., Roostaei, T., Nho, K., Risacher, S.L., Bradshaw, E.M., Petyuk, V., Schneider, J.A., Saykin, A., Bennett, D.A., and De Jager, P.L. (2019). Neuropathological correlates and genetic architecture of microglial activation in elderly human brain. Nat Commun *10*, 409. https://doi.org/10.1038/s41467-018-08279-3.

78. Kuan, P., Clouston, S., Yang, X., Che, C., Gandy, S., Kotov, R., Bromet, E., and Luft, B.J. (2021). Single-cell transcriptomics analysis of mild cognitive impairment in World Trade Center disaster responders. Alz & Dem Diag Ass & Dis Mo *13*, e12154. https://doi.org/10.1002/dad2.12154.

79. Craig, D.W., Hutchins, E., Violich, I., Alsop, E., Gibbs, J.R., Levy, S., Robison, M., Prasad, N., Foroud, T., Crawford, K.L., et al. (2021). RNA sequencing of whole blood reveals early alterations in immune cells and gene expression in Parkinson's disease. Nat Aging *1*, 734–747. https://doi.org/10.1038/s43587-021-00088-6.

80. Wong, C.W., Ziser, L., Sparke, L., Zhao, R., Freydenzon, A., Chauquet, S., Henderson, R., Ngo, S., Wallace, L., Wray, N.R., et al. (2025). A Blood Transcriptomic Resource for ALS Highlights Disease-Associated Signatures and Alternative Splicing Events. Preprint at Neurology, https://doi.org/10.1101/2025.07.28.25332310 https://doi.org/10.1101/2025.07.28.25332310.

81. Kyritsis, N., Torres-Espín, A., Schupp, P.G., Huie, J.R., Chou, A., Duong-Fernandez, X., Thomas, L.H., Tsolinas, R.E., Hemmerle, D.D., Pascual, L.U., et al. (2021). Diagnostic blood RNA profiles for human acute spinal cord injury. Journal of Experimental Medicine *218*, e20201795. https://doi.org/10.1084/jem.20201795.

## Figure legends

### Figure 1 : Ligand identity and dose tunes endogenous MyD88 assembly kinetics

**A**) Schematic of CRISPR/Cas9 edited full length mouse MyD88 with C-terminal mNeonGreen (mNG) tag.

**B**) Schematic of TIRF imaging of membrane proximal MyD88 assemblies.

**C**) Dose-dependent MyD88 assembly kinetics with (minimum 25 cells across all concentrations and ligands were analysed). Data represent mean ± SE (3 replicates).

**D**) Ridgeline charts of time-dependent intensity distribution of MyD88 assembly. At least 25 cells were analyzed per ligand at each time point, from 2 biological and 4 technical replicates in total.

**E**) Representative TIRF image and MyD88 masks showing heterogeneous MyD88 assembly in LPS (100 ng/ml) treated cells. Cells with higher and lower MyD88 assembly are marked as (i) and (ii) respectively, and zoomed insets are provided (scale bar 20 μm).

**F**) Dose-dependent distribution of cells between Group A and Group B, defined by the presence or absence of hexameric or larger MyD88 assemblies. Statistics similar to kinetics measurement.

**G**) Schematic representation of volumetric imaging of MyD88 assemblies.

**H**) Representative max-intensity projections of MyD88 assembly throughout the cell volume (scale bar 15 μm).

**I**) Ridgeline charts of time dependent MyD88 assembly formed throughout the cell volume. At least 1000 puncta were analysed per ligand at each time point (unstimulated with approximately 100).

**J**) Group stratification (group A and B) of total MyD88 assembly/cell across all three ligands. Data represent mean ± SD across 3 biological replicates (approximately 75, 128, and 121 cells per timepoint for LPS, MPLA, and $Pam_3CSK_4$ respectively). Across all ligands and time points, Group A and Group B cells were compared using a two-sided unpaired Student's *t* test, $*p < 0.05$, $**p < 0.01$, $***p < 0.001$, NS, not significant.

**Figure 2 : Pre-existing MyD88 abundance heterogeneity predicts single-cell MyD88 assembly capacity**

**A)** Schematic of single-cell FCS for freely diffusing MyD88-mNG.

**B)** Representative confocal image and fitted autocorrelation curves from two cells used to estimate absolute MyD88 concentration.

**C)** Distribution of MyD88 concentration across three biological replicates (25 cells total).

**D)** Representative immunofluorescence images of MyD88 in MyD88-mNG iBMDMs, WT iBMDMs, and primary BMDMs. White and beige arrows indicate bright and dim cells, respectively. Scale bar 20 μm.

**E)** Quantification of MyD88 heterogeneity as coefficient of variation (%). Data were collected from 3 animals (188 cells) for primary BMDMs, 2 biological replicates (192 cells) for WT iBMDMs, and 3 biological replicates (300 cells) for MyD88-mNG iBMDMs.

**F)** Micro-patterned imaging chambers with 200 μm diameter wells to image MyD88-mNG colony formation. Enhanced fluorescence profile of the bioinert surface enabling localization (scale bar 50 μm).

**G)** Redistribution of MyD88 intensity in colonies over 6 days until confluency (scale bar 50 μm).

**H**) Longitudinal heatmap of MyD88-mNG intensity heterogeneity, reported as %CV, across individual wells during colony growth.

**I)** Vybrant DyeCycle intensity distribution identifying broad cell-cycle phases, data collected over 3 biological replicates (361 cells).

**J)** MyD88-mNG intensity in cells from the two peaks in (**I**). The two distributions are not significantly different at the 0.05 level by Kolmogorov–Smirnov test.

**K)** Correlation between MyD88 assemblies and normalized total MyD88 intensity per cell after LPS (91 cells), MPLA (130 cells), or $Pam_3CSK_4$ (121 cells) stimulation. Spearman's ρ values are shown.

**Figure 3: Strong agonism converts MyD88 abundance into productive large assemblies**

**A**) Schematic of MyD88 assembly. The pathways include 1: Monomer-dimer equilibrium of TLR4-MD2 complex, 2: ligand induced dimer stabilization, 3: MyD88 recruitment to the receptor TIR domain, 4: Recruitment of IRAK(s) to generate functional MyD88 complex. These steps were analyzed using coarse-grained scaling that compares the dependence of small and large MyD88 assemblies on cellular MyD88 abundance. Scaling exponents for LPS- and MPLA-induced small and large assemblies are indicated.

**B**) Distribution of MyD88 concentration with LPS stimulation. Dashed lines indicate the three MyD88 bins.

**C-E**) Intensity distributions of MyD88 assemblies within the three MyD88 bins for LPS stimulation. Colours indicate empirically defined small and large assembly classes. Assembly intensities were normalized to average intensity of unstimulated MyD88 assemblies.

**F-G**) Double-logarithmic plots showing linear fits to extract scaling exponents of small **(F)** and large **(G)** MyD88 assemblies under LPS stimulation.

**H**) Distribution of MyD88 concentration with MPLA stimulation. Dashed lines indicate the three MyD88 bins.

**I-K**) Intensity distributions of MyD88 assemblies within the three MyD88 bins for MPLA stimulation. Colours indicate small and large assembly classes. Normalized assembly intensities differ from LPS because the measurements were acquired under separate experimental conditions.

**L-M**) Double-logarithmic plots showing linear fits to extract scaling exponents of small **(L)** and large **(M)** MyD88 assemblies under MPLA stimulation.

**Figure 4. MyD88 assembly state predicts NFκB activation and transcriptional output**

**A**) Schematic of the downstream signaling cascade, showing IKK complex activation, NFκB phosphorylation, IκBα degradation, nuclear translocation of Ser536-p65, and transcriptional activation.

**B**) Representative immunofluorescence images of intracellular Ser536-p65 in fixed cells at different time points after LPS stimulation. Scale bar 15 µm.

**C**) Quantification of whole-cell Ser536-p65 intensity over time after LPS and MPLA stimulation. A minimum of 35 cells for LPS and 68 cells for MPLA were analyzed per time point across 3 biological replicates. Data represent mean ± SD.

**D**) Representative 3D reconstruction of cell volume, nuclear volume, and MyD88 assemblies. Colour scales indicate total Ser536-p65 intensity within the nucleus, and mean intensity of MyD88 assemblies. Scale bar 7 µm.

**E**) Nuclear enrichment of Ser536-p65, expressed as the nucleus-to-cytoplasm intensity ratio, shown after group stratification. Cell numbers are the same as in (**C**). Data represent mean ± SD.

**F**) Schematic of the smFISH workflow used to quantify *NFKBIA* mRNA.

**G**) Representative images from smFISH measurements. Scale bar 10 µm.

**H**) Relative number of *NFKBIA* mRNA transcripts per cell after stimulation, measured by smFISH. A minimum of 354 cells for LPS and 542 cells for MPLA were analyzed per time point across 3 biological replicates. Data represent mean ± SD.

**Figure 5. MyD88 assembly state stratifies single-cell TNFα output**

**A**) Schematic of the time-window assay relating MyD88-dependent signaling to TNFα output. TAPI-0 was added at stimulation to prevent TNFα shedding and retain TNFα at the membrane. TAK-242 was added at the indicated times to block further TLR4-driven MyD88 assembly. TNFα was measured at 4 h in all conditions; therefore, TAK-242 timing defines the duration of allowed MyD88-dependent signaling before pathway inhibition.

**B**) Representative immunofluorescence images of membrane-anchored TNFα after LPS stimulation in the presence of TAPI-0. Scale bar 20 µm.

**C**) Ring-band quantification of membrane-anchored TNFα after LPS or MPLA stimulation as a function of TAK-242 addition time. At least 48 cells were analyzed per time point from 2 biological replicates. Data represent mean ± SD.

**D** – **E**) Dual-axis plots showing the average number of MyD88 assemblies per cell (mean ± SD from previous confocal measurements together with ΔTNFα, defined as mean TNFα ($t_n$- $t_{n-1}$) for **D**) LPS and **E**) MPLA stimulation.

**F**) Schematic of the assay used for simultaneous detection of MyD88 assemblies and intracellular TNFα using BFA.

**G**) Representative immunofluorescence images of antibody-stained MyD88 assemblies and TNFα in MyD88-mNG iBMDMs and primary BMDMs. Scale bar 20 µm.

**H**) Stratification of TNFα production in MyD88-mNG iBMDMs into two groups. Significance was assessed across the full distribution by Kolmogorov–Smirnov test (85 cells).

**I**) Number of MyD88 assemblies per cell in the two groups in MyD88-mNG iBMDMs. Significance was assessed by Student's *t* test (*$p < 0.05$). Data represent mean of 3 biological replicates.

**J**) Stratification of TNFα production in primary BMDMs into two groups. Significance was assessed across the full distribution by Kolmogorov–Smirnov test (193 cells).

**K**) Number of MyD88 assemblies per cell in the two groups in primary BMDMs. Significance was assessed by Student's *t* test (*$p < 0.01$). Data represent pooled technical replicates from 4 animals.

**Figure 6. Strong agonism couples MyD88-dependent activation to feedback engagement**

**A**) Cytokine persistence after LPS or MPLA stimulation, expressed as the ratio of TNFα or IL6 measured at 24 h relative to 4 h. Data represent mean ± SE from 6 and 4 biological replicates for LPS and MPLA, respectively. Significance was assessed using Kruskal-Wallis ANOVA, $*p < 0.05$.

**B**) Total MyD88 assembly per cell at later time points after LPS or MPLA stimulation. Data represent mean ± SD from 3 biological replicates, with at least 100 cells analyzed per time point. Significance was assessed using unpaired Student's *t* test, $*p < 0.05$.

**C**) Schematic of full-length MyD88 (MyD88L), and exon 2-skipped isoform MyD88s lacking the intermediate domain.

**D**) MyD88s/MyD88L ratio after LPS or MPLA stimulation at the indicated times. Data are distributions from 6 biological replicates for LPS, and 5 for MPLA. One-way ANOVA showed a significant increase only after 24 h LPS relative to unstimulated cells ($*p < 0.05$).

**E**) Heatmaps of negative regulators and cytokines/chemokines induced by LPS or MPLA at 4 h. Values represent mean from 6 biological replicates.

**F**) Volcano plot of differential expression, shown as log2 fold change (LPS/MPLA). Genes marked in blue and pink shades are statistically significant (adjusted $*p<0.05$) under MPLA and LPS stimulation respectively. Representative cytokines and negative regulators (highlighted in green) are expressed significantly higher with LPS stimulation.

**G**) Representative A20 immunofluorescence images in MyD88-mNG cells with LPS stimulation. Scale bar 30 µm.

**H**) Group-wise A20 intensity in LPS-stimulated cells (115 cells total). Significance was tested using unpaired Student's *t* test, $*p < 0.05$.

**Figure 7. AD pathology is associated with NFκB-linked activation without proportional transcriptional feedback engagement**

**A**) Schematic of the ROSMAP analysis workflow. Bulk RNAseq and single-nucleus RNAseq datasets from dorsolateral prefrontal cortex (DLPFC) were analyzed to relate inflammatory and negative-regulatory gene expression to Alzheimer's disease (AD)-associated pathology, including Braak stage, amyloid-β plaque burden, and tau tangle burden. Numbers indicate cohort sizes stratified by AD and non-disease control, and sex for bulk RNA-seq and snRNA-seq datasets.

**B**) Variance-stabilized expression of NFKBIA, MYD88s, TNFAIP3/A20, and SOCS3 across Braak stages from bulk RNA-seq analysis of DLPFC tissue showing. Differences in gene expression across Braak-stage groups were assessed by ANOVA, with p values shown in each panel.

**C**) Microglia-specific snRNA-seq analysis showing variance-stabilized expression of NFKBIA, MYD88s, TNFAIP3/A20, and SOCS3 across Braak stages. Differences in gene expression across Braak-stage groups were assessed by ANOVA, with p values shown in each panel.

**D**) Microglial expression of NFKBIA, MYD88s, TNFAIP3/A20, and SOCS3 plotted against square-root-transformed amyloid-β burden from snRNA-seq analysis. Associations were assessed using Pearson's correlation, with correlation coefficients shown as R and corresponding p values indicated in each panel.

**E**) Microglial expression of the same genes plotted against square-root-transformed tau tangle burden from snRNA-seq analysis. Associations were assessed using Pearson's correlation, with correlation coefficients shown as R and corresponding p values indicated in each panel.

**F)** Heat maps of population scaled Z-score values for selected set of genes in chronic inflammatory diseases.

**G**) Heat maps of population scaled Z-score values for selected set of genes in acute inflammatory diseases.

**H**) Δ Z-score values calculated as a difference between the scaled average Z-values of negative feedback and inflammatory module. Corresponding data points are individual diseases. Significance testing was done by one-way ANOVA ($p$ <0.00622).

**Figure 1**

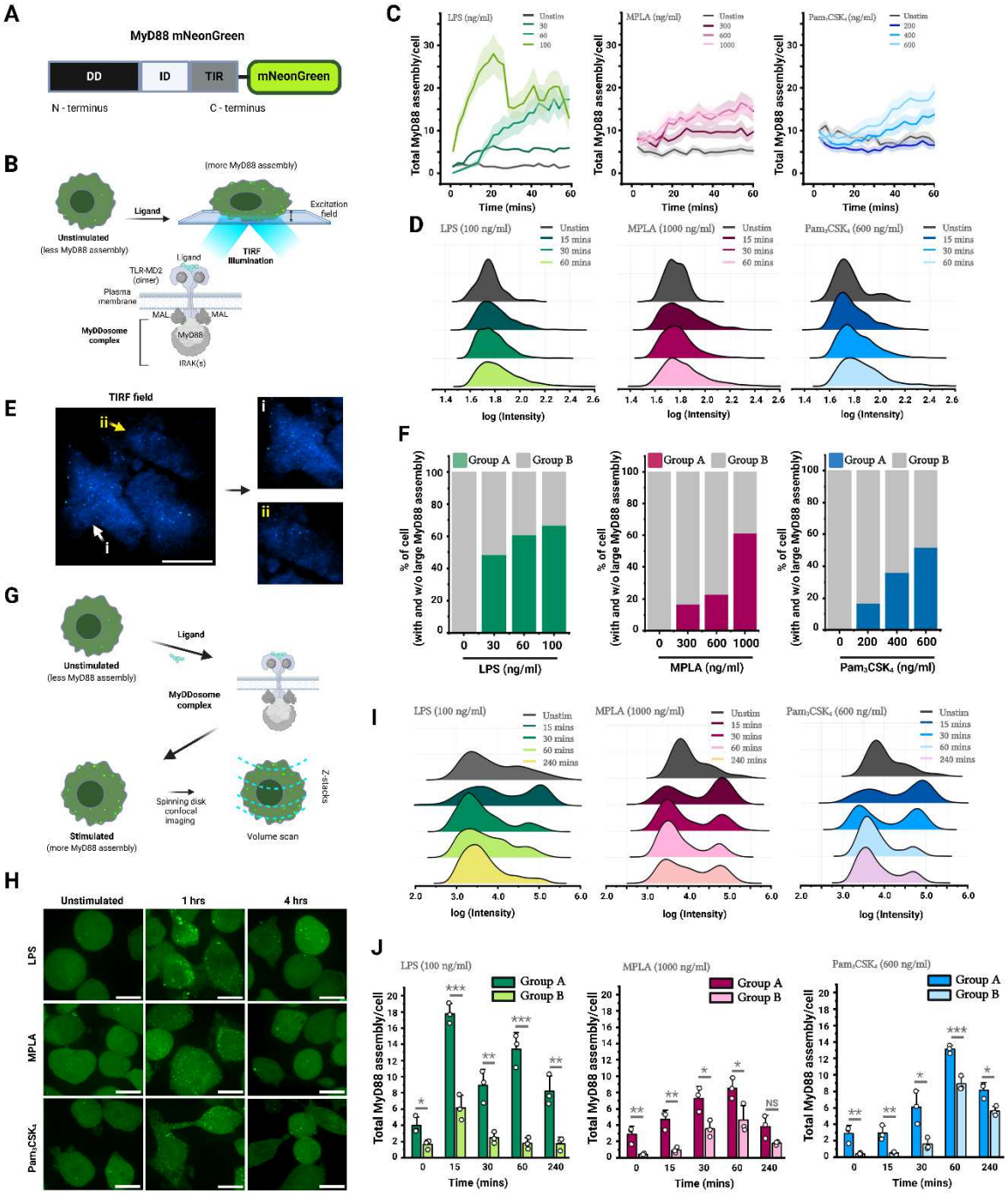

A
MyD88 mNeonGreen
DD
ID
TIR
mNeonGreen
N - terminus
C - terminus
B
(more MyD88 assembly)
Ligand
Excitation field
Unstimulated
(less MyD88 assembly)
TIRF Illumination
Ligand
TLR-MD2 (dimer)
Plasma membrane
MAL
MAL
MyDDosome complex
MyD88
IRAK(s)
C
LPS (ng/ml)
Unstim
30
60
100
MPLA (ng/ml)
Unstim
300
600
1000
Pam3CSK4 (ng/ml)
Unstim
200
400
600
Total MyD88 assembly/cell
Time (mins)
D
LPS (100 ng/ml)
MPLA (1000 ng/ml)
Pam3CSK4 (600 ng/ml)
Unstim
15 mins
30 mins
60 mins
log (Intensity)
E
TIRF field
i
ii
F
Group A
Group B
% of cell (with and w/o large MyD88 assembly)
LPS (ng/ml)
MPLA (ng/ml)
Pam3CSK4 (ng/ml)
G
Unstimulated
(less MyD88 assembly)
Ligand
MyDDosome complex
Stimulated
(more MyD88 assembly)
Spinning disk confocal imaging
Z steps
Volume scan
H
Unstimulated
1 hrs
4 hrs
LPS
MPLA
Pam3CSK4
I
LPS (100 ng/ml)
MPLA (1000 ng/ml)
Pam3CSK4 (600 ng/ml)
Unstim
15 mins
30 mins
60 mins
240 mins
log (Intensity)
J
LPS (100 ng/ml)
MPLA (1000 ng/ml)
Pam3CSK4 (600 ng/ml)
Group A
Group B
Total MyD88 assembly/cell
Time (mins)
NS

**Figure 2**

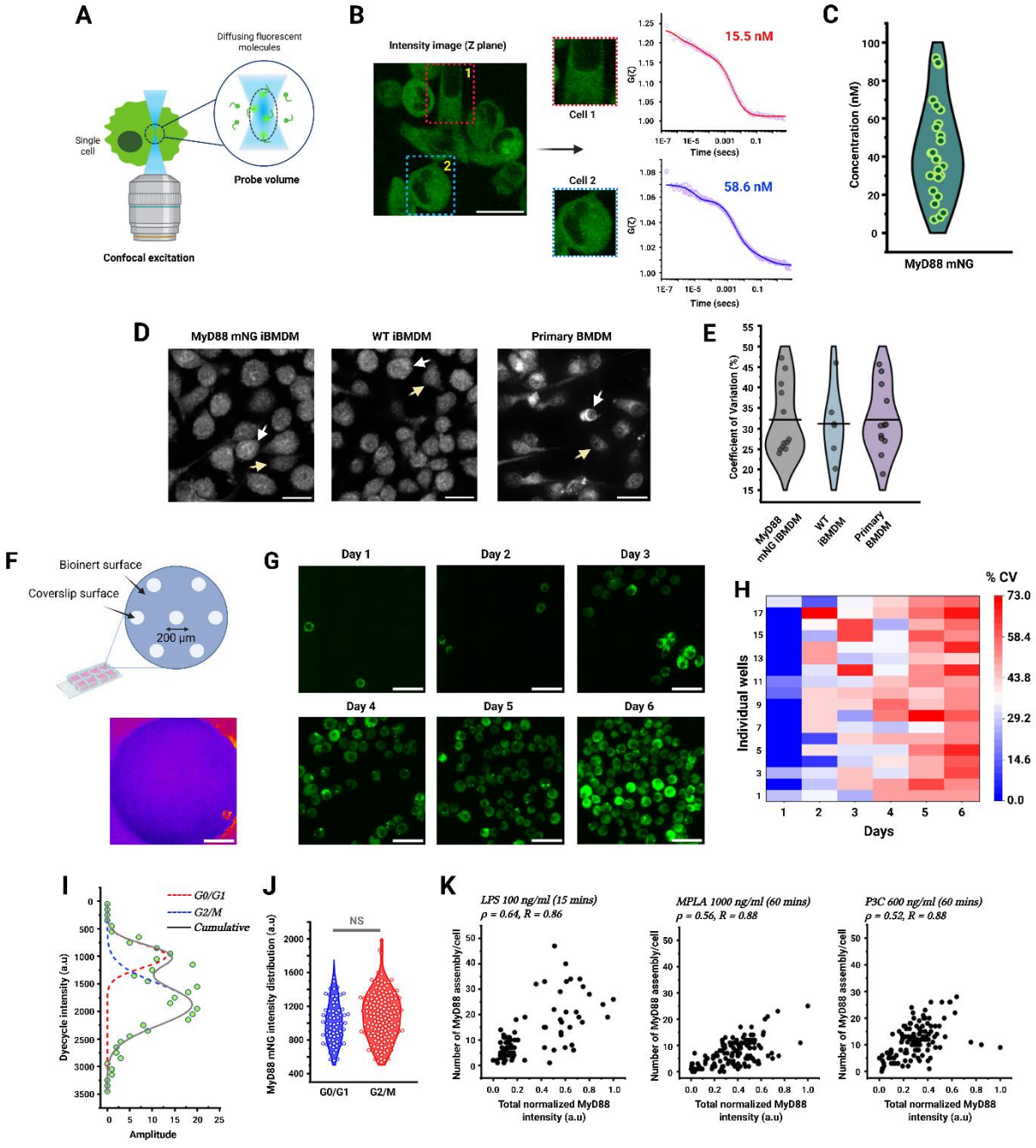

A
Diffusing fluorescent molecules
Single cell
Probe volume
Confocal excitation
B
Intensity image (Z plane)
Cell 1
Cell 2
15.5 nM
58.6 nM
G(τ)
Time (secs)
C
Concentration (nM)
MyD88 mNG
D
MyD88 mNG iBMDM
WT iBMDM
Primary BMDM
E
Coefficient of Variation (%)
MyD88 mNG iBMDM
WT iBMDM
Primary BMDM
F
Bioinert surface
Coverslip surface
200 µm
G
Day 1
Day 2
Day 3
Day 4
Day 5
Day 6
H
% CV
Individual wells
Days
I
G0/G1
G2/M
Cumulative
Dyecycle intensity (a.u)
Amplitude
J
NS
MyD88 mNG intensity distribution (a.u)
G0/G1
G2/M
K
LPS 100 ng/ml (15 mins)
ρ = 0.64, R = 0.86
MPLA 1000 ng/ml (60 mins)
ρ = 0.56, R = 0.88
P3C 600 ng/ml (60 mins)
ρ = 0.52, R = 0.88
Number of MyD88 assembly/cell
Total normalized MyD88 intensity (a.u)

**Figure 3**

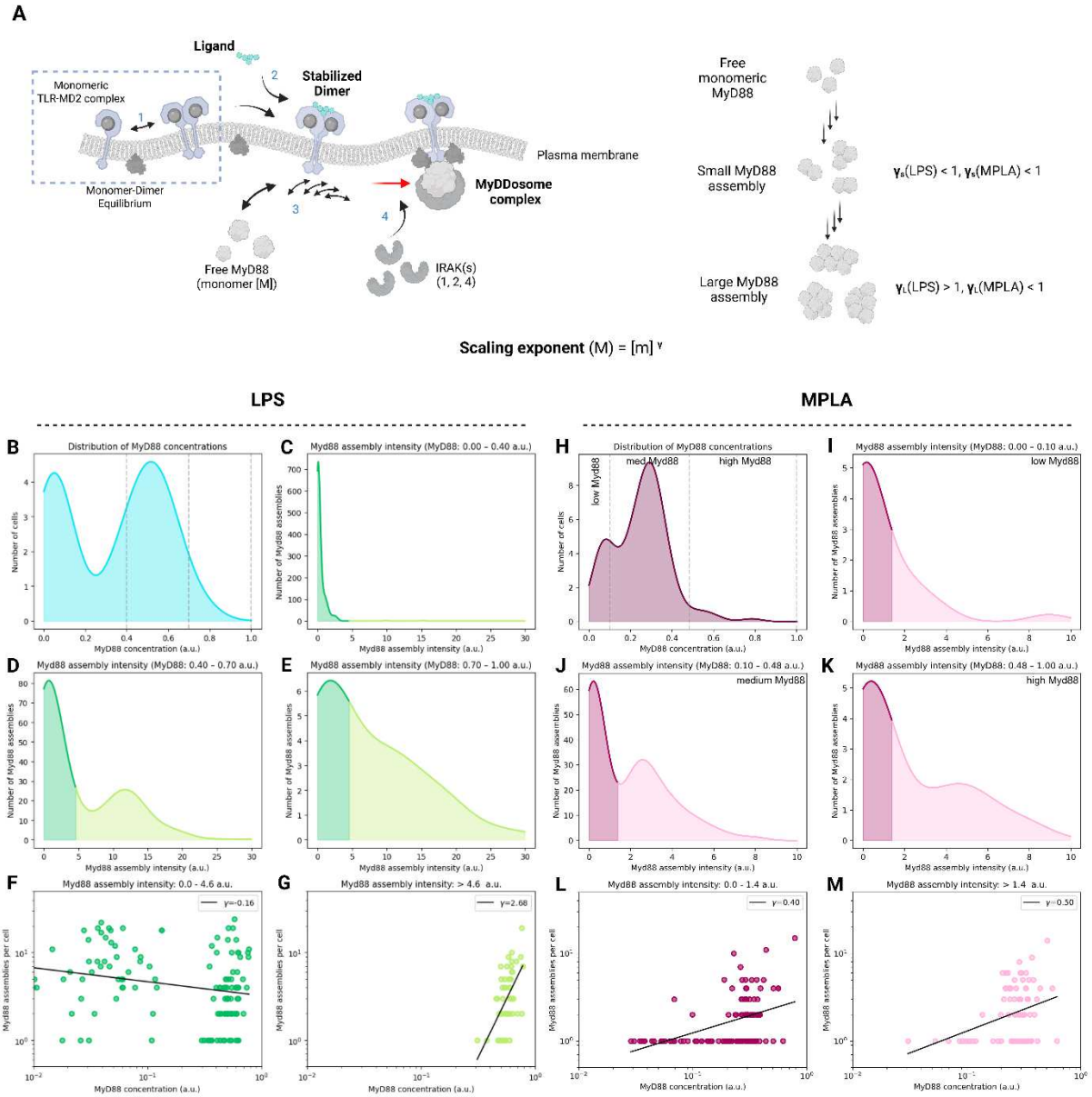
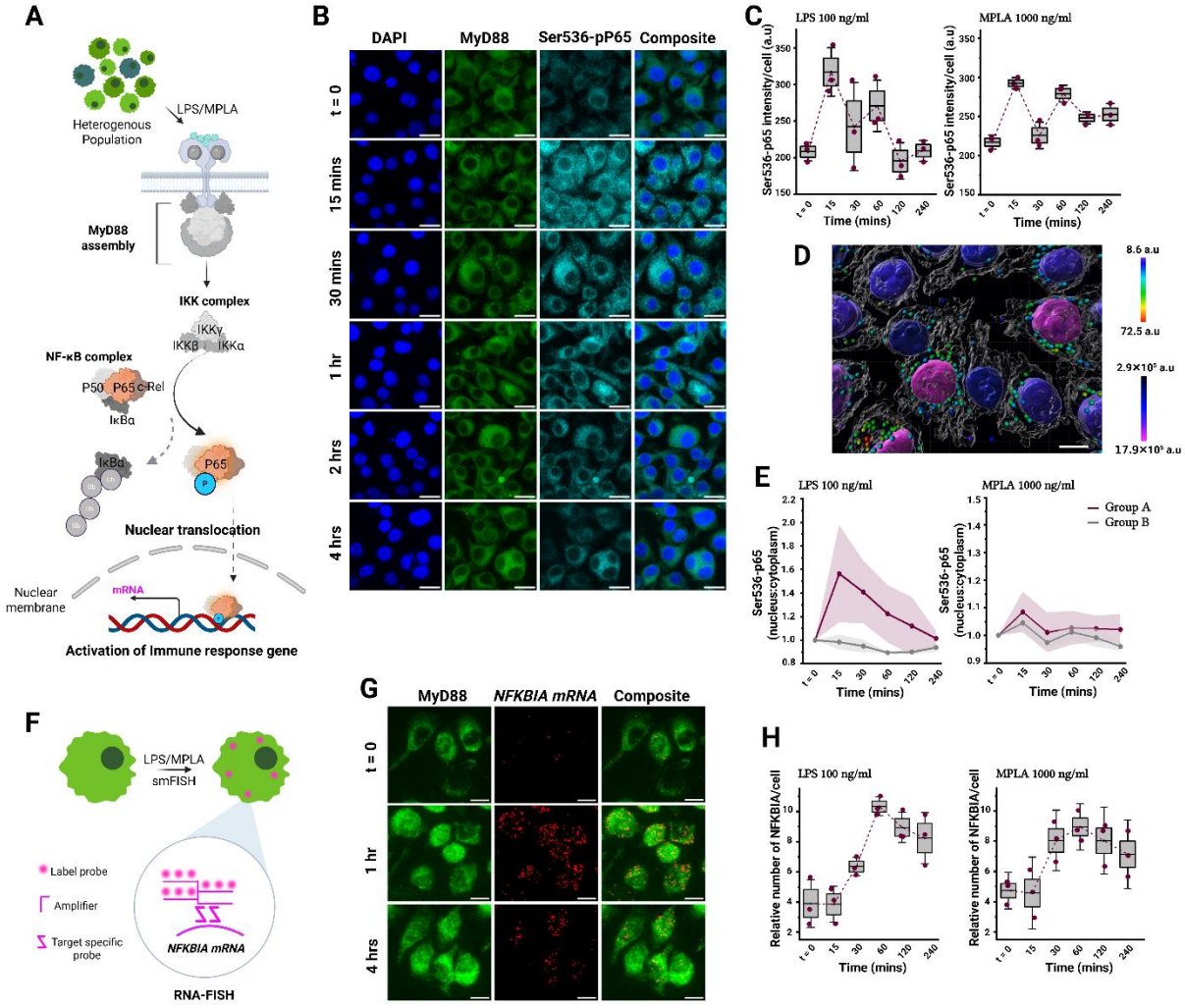

A
Ligand
Monomeric TLR-MD2 complex
Stabilized Dimer
Plasma membrane
Monomer-Dimer Equilibrium
MyDDosome complex
Free MyD88 (monomer [M])
IRAK(s) (1, 2, 4)
Free monomeric MyD88
Small MyD88 assembly
$\gamma_s$(LPS) < 1, $\gamma_s$(MPLA) < 1
Large MyD88 assembly
$\gamma_L$(LPS) > 1, $\gamma_L$(MPLA) < 1
Scaling exponent (M) = [m]$^{\gamma}$
LPS
MPLA
B Distribution of MyD88 concentrations
C Myd88 assembly intensity (MyD88: 0.00 - 0.40 a.u.)
H Distribution of MyD88 concentrations
I Myd88 assembly intensity (MyD88: 0.00 - 0.10 a.u.)
D Myd88 assembly intensity (MyD88: 0.40 - 0.70 a.u.)
E Myd88 assembly intensity (MyD88: 0.70 - 1.00 a.u.)
J Myd88 assembly intensity (MyD88: 0.10 - 0.48 a.u.)
K Myd88 assembly intensity (MyD88: 0.48 - 1.00 a.u.)
F Myd88 assembly intensity: 0.0 - 4.6 a.u.
G Myd88 assembly intensity: > 4.6 a.u.
L Myd88 assembly intensity: 0.0 - 1.4 a.u.
M Myd88 assembly intensity: > 1.4 a.u.
low Myd88
med Myd88
high Myd88
medium Myd88
Number of cells
Number of Myd88 assemblies
MyD88 concentration (a.u.)
Myd88 assembly intensity (a.u.)
Myd88 assemblies per cell
γ=-0.16
γ=2.68
γ=0.40
γ=0.50

**Figure 4**


A
Heterogenous Population
LPS/MPLA
MyD88 assembly
IKK complex
IKKγ
IKKβ
IKKα
NF-κB complex
P50
P65
c-Rel
IκBα
IκBα
P65
Nuclear translocation
Nuclear membrane
mRNA
Activation of Immune response gene
B
DAPI
MyD88
Ser536-pP65
Composite
t = 0
15 mins
30 mins
1 hr
2 hrs
4 hrs
C
LPS 100 ng/ml
MPLA 1000 ng/ml
Ser536-p65 intensity/cell (a.u)
Time (mins)
D
8.6 a.u
72.5 a.u
2.9×10⁵ a.u
17.9×10⁵ a.u
E
LPS 100 ng/ml
MPLA 1000 ng/ml
Group A
Group B
Ser536-p65 (nucleus:cytoplasm)
Time (mins)
F
LPS/MPLA
smFISH
Label probe
Amplifier
Target specific probe
NFKBIA mRNA
RNA-FISH
G
MyD88
NFKBIA mRNA
Composite
t = 0
1 hr
4 hrs
H
LPS 100 ng/ml
MPLA 1000 ng/ml
Relative number of NFKBIA/cell
Time (mins)

## Figure 5

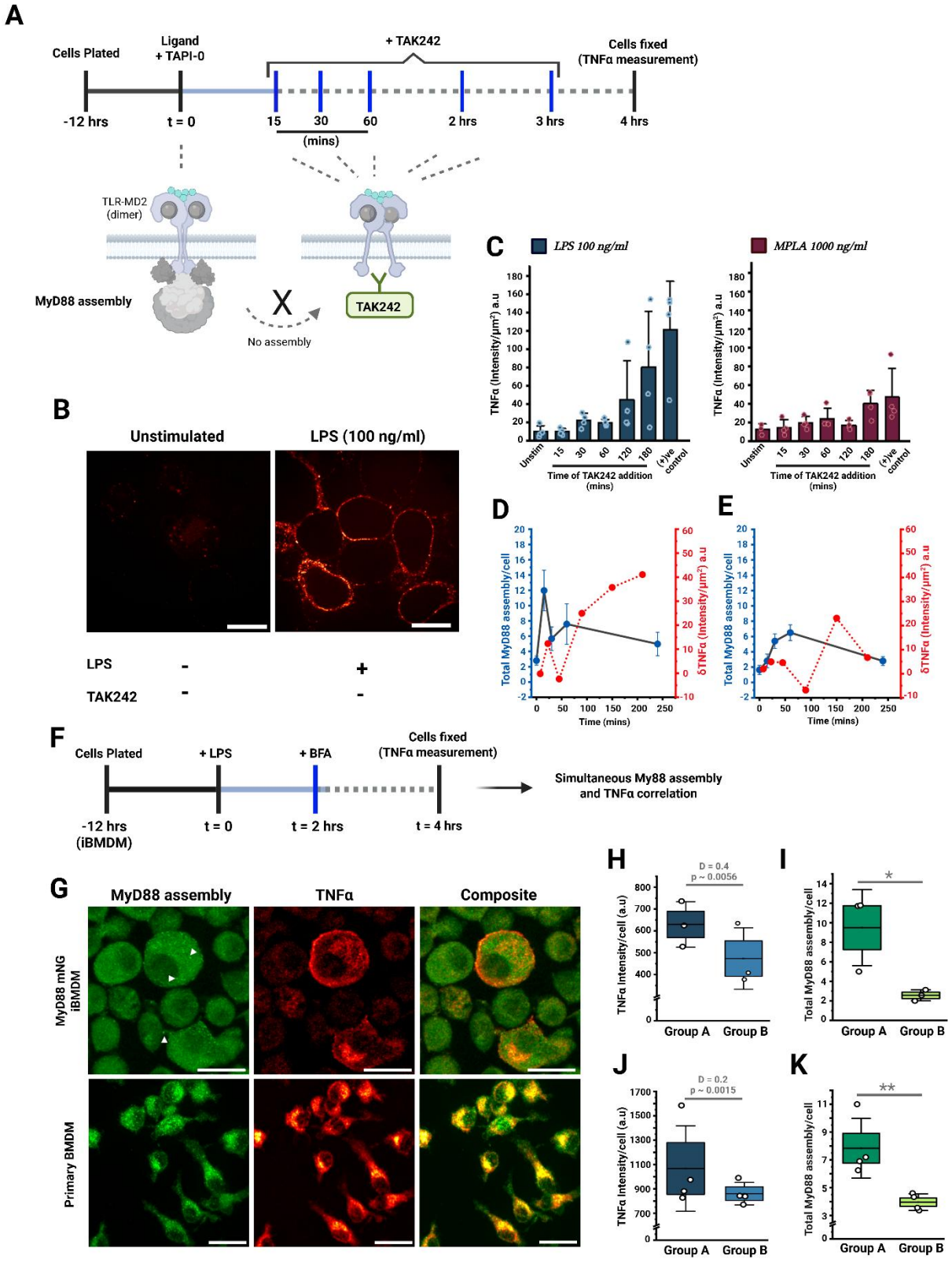

A
Cells Plated
Ligand + TAPI-0
+ TAK242
Cells fixed (TNFα measurement)
-12 hrs
t = 0
15
30
60
2 hrs
3 hrs
4 hrs
(mins)
TLR-MD2 (dimer)
MyD88 assembly
X
No assembly
TAK242
B
Unstimulated
LPS (100 ng/ml)
LPS - +
TAK242 - -
C
LPS 100 ng/ml
MPLA 1000 ng/ml
TNFα (Intensity/μm²) a.u
Unstim
15
30
60
120
180
(+)ve control
Time of TAK242 addition (mins)
D
E
Total MyD88 assembly/cell
δTNFα (Intensity/μm²) a.u
Time (mins)
F
Cells Plated
+ LPS
+ BFA
Cells fixed (TNFα measurement)
-12 hrs (iBMDM)
t = 0
t = 2 hrs
t = 4 hrs
Simultaneous My88 assembly and TNFα correlation
G
MyD88 assembly
TNFα
Composite
MyD88 mNG iBMDM
Primary BMDM
H
D = 0.4
p ~ 0.0056
TNFα Intensity/cell (a.u)
Group A
Group B
I
*
Total MyD88 assembly/cell
J
D = 0.2
p ~ 0.0015
K
**

**Figure 6**

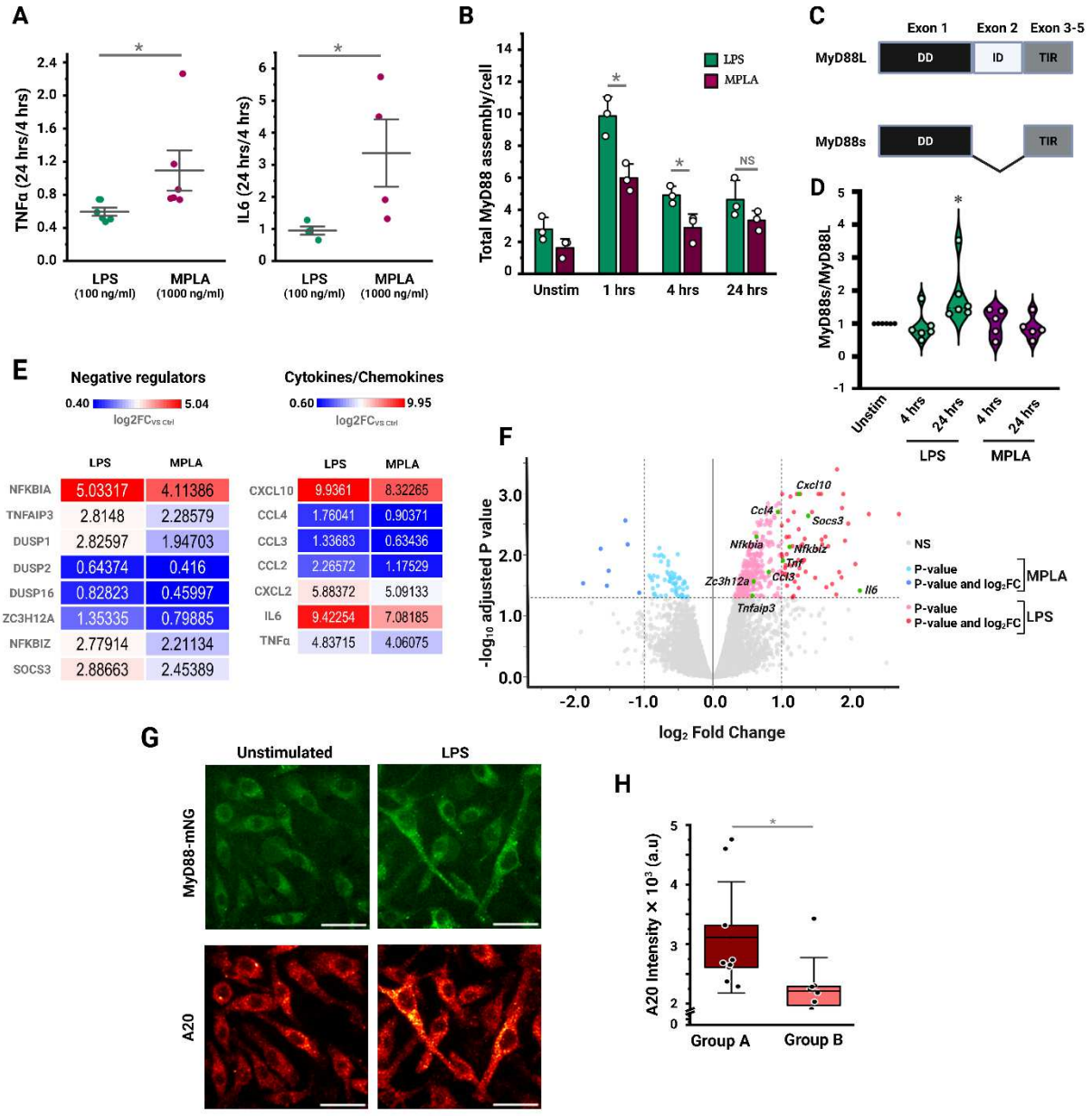
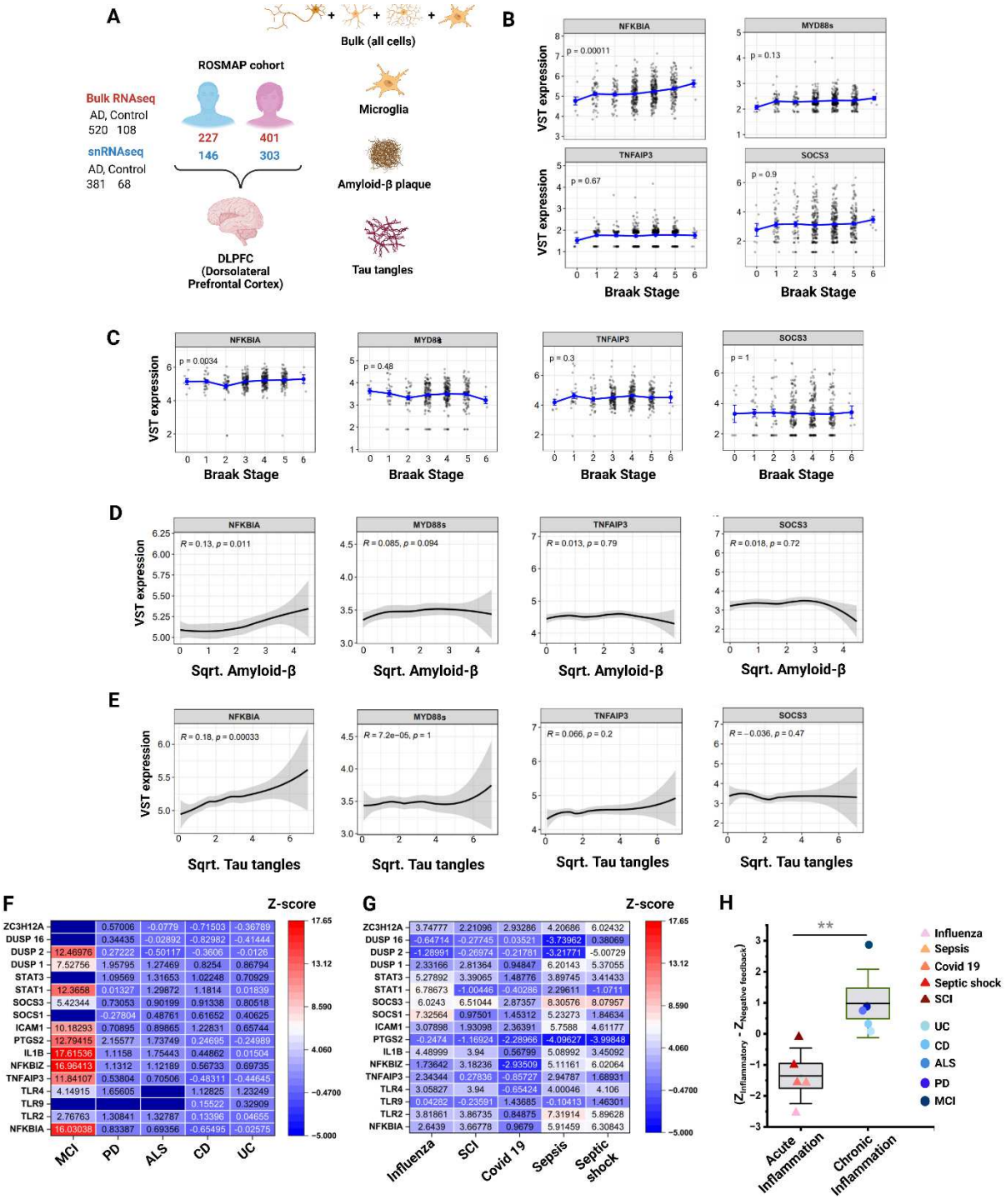

A
TNFα (24 hrs/4 hrs)
IL6 (24 hrs/4 hrs)
LPS (100 ng/ml)
MPLA (1000 ng/ml)
B
Total MyD88 assembly/cell
LPS
MPLA
Unstim
1 hrs
4 hrs
24 hrs
NS
C
Exon 1
Exon 2
Exon 3-5
MyD88L
DD
ID
TIR
MyD88s
DD
TIR
D
MyD88s/MyD88L
Unstim
4 hrs
24 hrs
4 hrs
24 hrs
LPS
MPLA
E
Negative regulators
0.40
5.04
log2FC vs ctrl
Cytokines/Chemokines
0.60
9.95
log2FC vs ctrl
LPS
MPLA
NFKBIA 5.03317 4.11386
TNFAIP3 2.8148 2.28579
DUSP1 2.82597 1.94703
DUSP2 0.64374 0.416
DUSP16 0.82823 0.45997
ZC3H12A 1.35335 0.79885
NFKBIZ 2.77914 2.21134
SOCS3 2.88663 2.45389
CXCL10 9.9361 8.32265
CCL4 1.76041 0.90371
CCL3 1.33683 0.63436
CCL2 2.26572 1.17529
CXCL2 5.88372 5.09133
IL6 9.42254 7.08185
TNFα 4.83715 4.06075
F
-log10 adjusted P value
log2 Fold Change
Cxcl10
Ccl4
Socs3
Nfkbia
Nfkbiz
Tnf
Ccl3
Zc3h12a
Il6
Tnfaip3
NS
P-value
P-value and log2FC
MPLA
P-value
P-value and log2FC
LPS
G
Unstimulated
LPS
MyD88-mNG
A20
H
A20 Intensity × 10³ (a.u)
Group A
Group B

**Figure 7**


A
Bulk (all cells)
ROSMAP cohort
Bulk RNAseq
AD, Control
520 108
227 401
snRNAseq
AD, Control
381 68
146 303
Microglia
Amyloid-β plaque
Tau tangles
DLPFC
(Dorsolateral
Prefrontal Cortex)
B
NFKBIA
MYD88s
TNFAIP3
SOCS3
VST expression
Braak Stage
C
D
Sqrt. Amyloid-β
E
Sqrt. Tau tangles
F
Z-score
MCI
PD
ALS
CD
UC
G
Influenza
SCI
Covid 19
Sepsis
Septic shock
H
Acute Inflammation
Chronic Inflammation
Influenza
Sepsis
Covid 19
Septic shock
SCI
UC
CD
ALS
PD
MCI

## Supplementary Files

This is a list of supplementary files associated with this preprint. Click to download.

- SupportingInformation.docx
- 4HMPLAvs4HLPSdge.csv
- Naivevs4HMPLAdge.csv
- Naivevs4HLPSdge.csv